Progress in Oceanography 219 (2023) 103160

Contents lists available at ScienceDirect

Progress in Oceanography

journal homepage: www.elsevier.com/locate/pocean

Assessing net primary production in the northwestern Barents Sea using in situ, remote sensing and modelling approaches

Laura Castro de la Guardia [a,*], Tania Hernández Fariñas [b], Christian Marchese [c,d], Martí Amargant-Arumí [e], Paul G. Myers [f], Simon Bélanger [g], Philipp Assmy [a], Rolf Gradinger [e], Pedro Duarte [a]

[a] Norwegian Polar Institute, Fram Centre, Tromsø, Norway
[b] Ifremer, Normandy, France
[c] University of British Columbia, British Columbia, Canada
[d] University of Victoria, British Columbia, Canada
[e] UiT, The Arctic University of Norway, Tromsø, Norway
[f] University of Alberta, Edmonton, Alberta, Canada
[g] Université Québec à Rimouski, Quebec, Canada

ARTICLE INFO

Dataset link: https://doi.org/10.21335/NMDC-1371694848, https://hermes.acri.fr/index.php?class=archive, https://doi.org/10.5067/7Q8HCCWS4I0R, https://doi.org/10.48670/moi-00003, https://doi.org/10.48670/moi-00001, http://knossos.eas.ualberta.ca/anha/model.php

Keywords:
Net primary production
Northwestern Barents Sea
Bioregionalization
Nansen Legacy

ABSTRACT

The northwestern Barents Sea (NW-BS) is a highly productive region within the transitional zones of an Atlantic to Arctic-dominated marine ecosystem. The steep latitudinal gradients in sea ice concentration, Atlantic and Arctic Water, offer an opportunity to test hypotheses on physical drivers of spatial and temporal variability of net primary production (NPP). However, quantifying NPP in such a large ocean region can be challenged by the lack of in situ measurements with high spatial and temporal resolution, and gaps in remote sensing estimates due to the presence of clouds and sea ice, and assumptions regarding the depth distribution of alga biomass. Without reliable data to evaluate models, filling these gaps with numerical models is limited by the model representation of the physical environment and its assumptions about the relationships between NPP and its main limiting factors. Hence, within the framework of the Nansen Legacy Project, we combined in situ measurements, remote sensing, and model simulations to constrain the estimates of phytoplankton NPP in the NW-BS. The region was subdivided into Atlantic, Subarctic, and Arctic subregions on the basis of different phytoplankton phenology. In 2004 there was a significant regime change in the Atlantic subregion that resulted in a step-increase in NPP in tandem with a step-decrease in sea ice concentration. Contrary to results from other Arctic seas, this study does not find any long term trends in NPP despite changes in the physical environment. Mixing was the main driver of simulated annual NPP in the Atlantic subregion, while light and nutrients drove annual NPP in the Subarctic and Arctic subregions. The multi-source estimate of annual NPP ranged 79–118 $gC\,m^{-2}\,yr^{-1}$ in the Atlantic, 74–82 $gC\,m^{-2}\,yr^{-1}$ in the Subarctic, and 19–47 $gC\,m^{-2}\,yr^{-1}$ in the Arctic. The total NPP in the NW-BS region was estimated between 15 and 48 $Tg\,C\,yr^{-1}$, which is 15–50% of the total NPP needed to sustain three of the most harvested fish species north of 62°N (roughly 90 $Tg\,C\ yr^{-1}$). This research shows the importance of continuing to strive for better regional estimates of NPP.

1. Introduction

The Barents Sea is a highly productive marginal shelf sea of the Arctic Ocean (Wassmann et al., 2006a). The physical environment is regionally structured by distinct distributions of Atlantic Water (AW), Arctic Water (ArW), and a seasonal sea ice cover (e.g., Loeng, 1991; Efstathiou et al., 2022). The resulting ocean stratification is generally weak and thermally driven in the south, while strong and salinity driven in the north (Wassmann et al., 2006a; Silva et al., 2021; Lundesgaard et al., 2022). The heterogeneity of the physical environment drives spatial and temporal patterns in the structure of the food web and biodiversity patterns (e.g., Søreide et al., 2003; Wassmann et al., 2006a; Kortsch et al., 2019). Environmental gradients are particularly steep in the northwestern Barents Sea (NW-BS). The south of the NW-BS is generally ice free and dominated by relatively warm and salty AW inflow (Loeng, 1991; Efstathiou et al., 2022). In contrast, the north

* Corresponding author.
E-mail addresses: laura.delaguardia@npolar.no, laura.delaguardia@gmail.com (L. Castro de la Guardia).

https://doi.org/10.1016/j.pocean.2023.103160

Available online 18 November 2023

Table 1
Nomenclature.

Abrev.	Definition
NPP	Regional-averaged Net Primary Production integrated over depth (0–100 m) and time (gC m^{-2} $time^{-1}$).
Chl-a	Chlorophyll-a concentration (mg m^{-3}). Averaged between 0–30 m depth for cross-comparison analysis, or between 0–100 m depth for bioregionalization analysis.
Nutr	Macronutrient concentration (mmol m^{-3}). Averaged over depth (0–100 m), time and area.
T	Temperature (°C). Averaged over depth (0–100 m), time, and area.
MXD	Seasonal maximum mixing layer depth (m). Averaged over area. Seasonal periods considered: Annual, Spring, Summer, Autumn. Sign convention is positive downward (e.g., larger positive numbers represent deeper MXD).
PAR	Photosynthetically available radiation (W m^{-2}): irradiance integrated between 400 and 700 nm wavelengths. Averaged over time, area and mixing layer depth.
SIC	Sea ice concentration (%). Averaged over time and area.
snowH	Snow depth (m). Averaged over time and area.
iceH	Sea ice thickness (m). Averaged over time and area.
Lys	Total number of days with light (days). Measured as number of days with PAR > 0 W m^{-2}.
OWL	Total number of Open Water days with Light (days). Measured as number of open water days (SIC < 10%) with some light (PAR > 0 W m^{-2})
AWz0	Atlantic Water volume (m^3) between the depth of 0 and 100 m. Averaged over time and area.
AWz100	Atlantic Water volume (m^3) between the depth of 100 and 200 m. Averaged over time and area.

AW was defined using potential density (range 27.7–27.97 kg m^{-3}) and conservative temperature greater than 2 °C (Rudels et al., 2000).

is seasonally ice-covered and dominated by an upper ocean inflow of fresher and colder ArW (Loeng, 1991; Reigstad et al., 2002; Koul et al., 2022), with a minor influence of AW carried eastward along the shelf break north of Svalbard and branching off at subsurface depths to enter the NW-BS (Lind and Ingvaldsen, 2012; Lundesgaard et al., 2022).

Regional patterns in net primary production (NPP) follow the general distribution of sea ice concentration (SIC) and water masses. Both NPP and secondary production typically are higher in AW relative to ArW-influenced regions (e.g., Rey, 1991; Reigstad et al., 2002; Basedow et al., 2014). Model estimates of annual gross primary production (GPP) suggest that the Barents Sea can be subdivided into three subregions: (i) a high GPP domain in the ice-free area, (ii) a moderate GPP domain in the seasonal ice-covered area, and (iii) a low GPP domain in permanently ice-covered area (Wassmann et al., 2010; Wassmann, 2011). However, considering the locally pronounced climate variability (Dalpadado et al., 2014), a bioregonalization of the NW-BS based on phytoplankton phenology would add crucial information about the temporal variability of phytoplankton, which may serve better to understand the physical drivers of NPP (Ardyna et al., 2017; Marchese et al., 2019; Silva et al., 2021; Marchese et al., 2022).

The NW-BS has experienced climate change related progressive warming (1981–2020) of the sea surface temperature (0.25 °C $decade^{-1}$; Mohamed et al., 2022b) and air temperature (ca. 2.7–4 °C $decade^{-1}$; Isaksen et al., 2022). Regional losses in SIC (ca. 15–10% $decade^{-1}$; Isaksen et al., 2022) and longer open water period (ca. 3.4-months; Mohamed et al., 2022a) have lead to higher underwater photosynthetic available radiation (PAR; Bélanger et al., 2013). These changes can strongly influence the spatial and temporal patterns of marine primary producers (Leu et al., 2015) and throughout the Arctic, they have led to a positive response of NPP (Dalpadado et al., 2014; Renaut et al., 2018; Lewis et al., 2020).

The fundamental role of NPP in the fuelling of food webs and carbon uptake makes it a central measure of ecosystem functioning and an important indicator of the effects of climate change. However, upscaling of marine NPP over large regions is challenging due to the lack of in situ measurements at high spatial and temporal resolution. Therefore, upscaling methods necessarily involve some knowledge about the relationships between NPP and its main limiting factors, as well as about the variability of such factors. These methods may be based on remote sensing or modelling techniques. However, while long-time series of remote sensing chlorophyll-a (Chl-a) and NPP could be obtained by combining data from the first ocean colour sensor, namely the Coastal Zone Colour Scanner (CZCS, 1979–1986), with the data (1998– ongoing) from more recent and modern sensors (Oziel et al., 2022), they are significantly limited in areas with sea ice and cloud cover. In such cases, numerical models become necessary tools that support the study of seasonality and interannual variability in NPP (Wassmann et al., 2006a).

Both "pure" modelling techniques and remote sensing-based algorithms (also partly based on modelling techniques) rely on a number of highly uncertain assumptions. Moreover, it is difficult, if possible, to evaluate the results of upscaling exercises, except by comparisons of calculated values and observations that may be available only at limited spatial and temporal coverage, due to the logistical challenges of measuring NPP. Therefore, we argue that using different approaches may help constrain NPP estimates in a manner analogous to the usage of modelling ensembles, allowing for some cross-validation of obtained results. Consistent with this, we combine in situ NPP measurements with remote sensing and model-based NPP estimates to quantify phytoplankton NPP in NW-BS and to analyse its temporal (over > 40 years) and spatial variability.

We subdivide the NW-BS based on a bioregionalization analysis with simulated Chl-a concentration. We produce a range of regional estimates of climatology, annual, and seasonal NPP employing a combination of different techniques from multiple sources. A 42-yearlong simulation was used to test the hypothesis of increasing phytoplankton NPP in the NW-BS related to recent climate change and identify physical drivers (listed in Table 1) in defined subregions (e.g., Reigstad et al., 2002; Wassmann, 2011). This study is part of The Nansen Legacy project (https://arvenetternansen.com), the collective effort of the Norwegian research community to get a more holistic understanding of the environmental and ecosystem changes witnessed in the Barents Sea.

2. Methods

The NW-BS is defined as the area between 75–84°N and 20–40°E (Fig. 1). The multi-source data for Chl-a and NPP are derived from in situ stations, remote sensing, and two coupled physical–biological ocean models. Temporal and spatial resolution varied with the data and output (Table 2). This section follows with a brief description of the datasets and the methods used to analyse them. Additional details pertaining to the origin of the data and output and how they were processed are included in the Appendix (Text A1).

2.1. In situ data

Chl-a and NPP were measured along a south–north transect that crossed the region defined as NW-BS (Fig. 1; Table 11). Water samples were taken at discrete depths (10, 20, 40, 60, 90 m, and Chl-a maximum) at the same stations for one or more years (2018, 2019, and 2021) between spring and summer. In situ, Chl-a was measured at stations P1–P5 in 2018–2021, P6 and P7 in 2019 and 2021, PICE in 2018, and SICE in 2019. These data were extracted from the database of the Norwegian Marine Data Centre (NMDC) established through The Nansen Legacy (Vader, 2022). NPP was measured at stations P1, P2, P4 and

Table 2
Overview of the NPP and Chl-a data sets with a period of available data, temporal and spatial resolution, and source information.

	In situ	MODIS-A	Takuvik	TOPAZ	BLING
Data type	Measurement	Remote sensing	Remote sensing	Model	Model
Period	2018–2021	2003–2021	2003–2011	2019–2021	1980–2021
Grid size	Punctual	4 km	9 km	6.25 km	12 km
Time	Punctual	Daily	Daily	Daily	5-day averages
Access	Link A	Link B	Link C	Link D	Link E

Link A (https://doi.org/10.21335/NMDC-1371694848); Link B (https://doi.org/10.5067/AQUA/MODIS/L3M/CHL/2022); Link C (http://www.takuvik.ulaval.ca/); Link D (https://doi.org/10.48670/moi-00003); Link E (http://knossos.eas.ualberta.ca/anha/model.php).

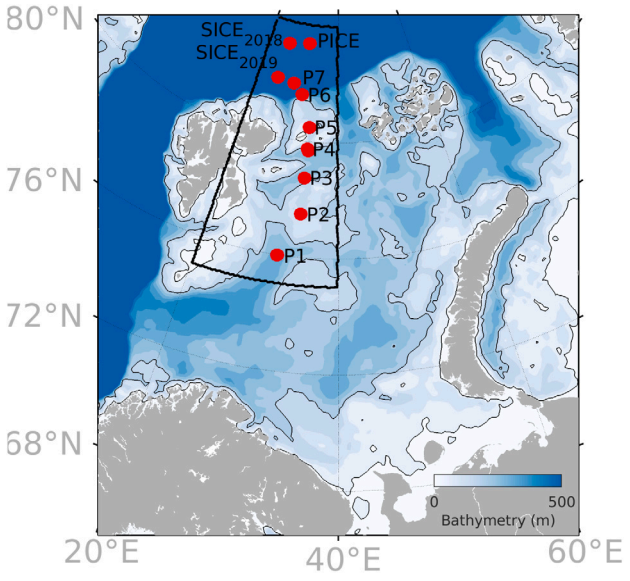

Fig. 1. Northwestern Barents Sea (NW-BS) polygon outlined in black (75–84°N and 20–40°E), and the Nansen Legacy sampling stations (red circles). The background colour is the regional bathymetry (m).

PICE in 2018 and P1, P4–P7 in 2019 and are analysed in an interannual 2018/2019 comparison study in Amargant-Arumi et al. (2023). The analysis followed standard procedures (The Nansen Legacy, 2022) with specific details listed in the appendix (Text A). These data were used for cross-validation with remote sensing and model estimates.

2.2. Remote sensing data

Time series of surface Chl-a (2002–2021) were derived from the Moderate Resolution Imaging Spectroradiometer sensors on board the Aqua satellite (MODISA; Hu et al., 2012). The time series of depth-integrated NPP (2003–2011) was produced by the Takuvik model from the Université du Québec à Rimouski (UQAR)- Takuvik International research group. The Takuvik NPP model was chosen for this study because it is spectrally resolved and specially tuned for Arctic Waters (e.g., Bélanger et al., 2013; Huot et al., 2013; Vernet et al., 2021; Mayot et al., 2020). The model derives NPP from remote-sensing Chl-a in surface waters that is projected downward to 100 m water depths assuming a Gaussian vertical distribution based on statistical analysis and phenology (Ardyna et al., 2013). The Takuvik model incorporates other remote sensing products (e.g., clouds, ozone, and sea ice concentration and in-water diffuse attenuation coefficient) to estimate PAR in the water column and derive critical parameters of phytoplankton NPP (Bélanger et al., 2013). NPP estimates consider only light limitation and assume that Nutr limitation is implicit from the Chl-a concentrations.

The accuracy of the remote sensing data depends on good visibility of the surface ocean, which is negatively affected by clouds and sea ice cover. Between 1993 and 2022, NW-BS experienced high cloud and ice cover, with >70% of the sea surface covered by sea ice or clouds each month (Figure 1.1). The average fraction of cloud and ice cover over the same period was >80% throughout the region (Fig. 2a). Consequently, there are large temporal and spatial gaps in the Chl-a and NPP data from remote sensing. On average, there are only 4 to 5 months per year (of a possible 10 months with sufficient daylight) with at least one day of available data in the southern parts of NW-BS (latitudes 75–78°N), while none to less than 3 months with data are represented above 79°N (Fig. 2b–c).

To achieve greater temporal and spatial coverage for the NPP estimates, it is common practice to fill in the gaps. These gaps are commonly addressed by careful spatio-temporal aggregation (Oziel et al., 2022), using monthly means (Bélanger et al., 2013) or by other methods that use information on the dominant spatial and temporal patterns (Marchese et al., 2017). The Takuvik simulation used in this study did not fill the gaps and serves to highlight the temporal and spatial limitations of remote sensing estimates (Fig. 3).

2.3. Coupled physical–biogeochemical model output

We used two state-of-the-art coupled ocean and biogeochemical models, BLING (Biology Light Iron Nutrient and Gas) and TOPAZ (Tracers of Phytoplankton with Allometric Zooplankton), to provide the evolution of essential biogeochemical variables along with the changing physical environment. The physical and biological components in both physical models are coupled online with the same timestep, using a one-way coupling. Models were used to explore cause-and-effect relationships and disentangle the effects of environmental changes on biological processes. The model output was also used to upscale NPP and to fill temporal gaps in the seasonal cycle of in situ and remote sensing NPP. We follow with a discussion of similarities and differences between the models and remote sensing and a brief description of the models (more details are given in the Appendix Text A).

One of the main differences between remote sensing and model-derived NPP is that the former is based on remotely observed Chl-a concentrations, combined with simplified assumptions about their vertical distribution, whereas the latter is based on simulated Chl-a concentrations. In both cases, Chl-a concentrations or another biomass proxy (e.g., phytoplankton carbon or nutrient concentration, here designated generically by [Phy]) are used to calculate the areal production from known response functions of the production rates normalized to biomass, with limiting factors such as light, temperature, and nutrients (Nutr). However, while remote sensing-based algorithms keep updating Chl-a concentrations over time from available measurements, coupled physical–biogeochemical models calculate phytoplankton biomass using the mass conservation equation (Eq. (1)). The model calculations are thus, based on regional advection and turbulent exchanges, and on biogeochemical gains and losses such as photosynthesis, respiration, sinking, mortality, etc. (Eq. (1)). In some models, biomass is expressed as carbon (or Nutr) concentration, which can be converted to Chl-a using known conversions or algorithms relating [Phy] production to Chl-a concentration (e.g.; Cloern et al., 1995). Thus, one may argue that there is an extra layer of uncertainty related to Chl-a variability.

$$\frac{\Delta[Phy]}{\Delta t} + \nabla(v.[Phy]) = \nabla(\lambda.\nabla[Phy]) + (\mathrm{Prod} - \mathrm{Met} - \mathrm{Sink} - \mathrm{Mort}).[Phy]$$

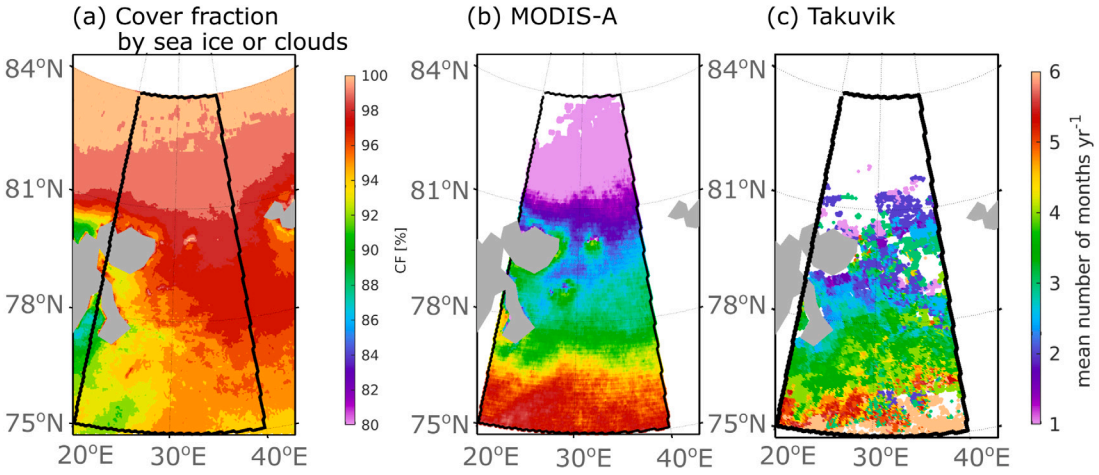

Fig. 2. Illustration of cloud and sea ice cover and associated gaps in the remote sensing data. (a) The percentage of the surface ocean covered by sea ice or clouds averaged between 1993–2022 (from https://hermes.acri.fr/index.php?class=archive). Number of months per year with at least one day available (b) MODIS-A Chl-a time series (2003–2021) and (c) Takuvik NPP (2003–2011).

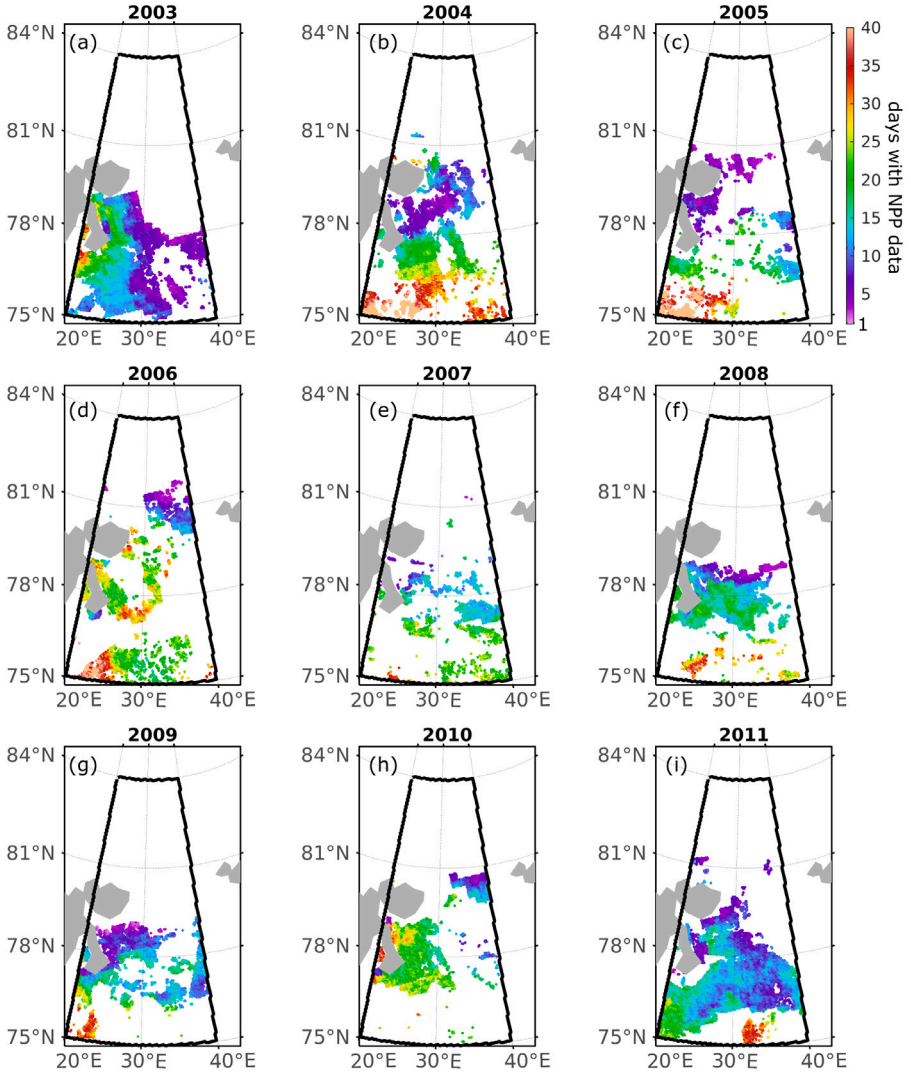

Fig. 3. Number of days per year with NPP data available within the NW-BS. Derived from Takuvik simulation without filling gaps in the remote sensing data.

(1)

where, the (∇) operator is a first-order spatial derivation, $\frac{\delta}{\delta x} + \frac{\delta}{\delta y} + \frac{\delta}{\delta z}$. The second term on the left side and the first term on the right side of Eq. (1) represent the advective and turbulent transport of [Phy], respectively. The remaining terms represent the rates of photosynthetic production (Prod), metabolism (Met), cell sinking (Sink), and mortality (Mort). Prod is typically calculated using response functions for light, temperature, and Nutr, which differ between models and remote sensing.

In this paper, TOPAZ output refers to the output of TOPAZ5-ECOSMO physical and biological reanalysis between 2019 and 2021. TOPAZ was chosen because it incorporates weekly assimilation of observations that are available in near real-time from in situ profilers and remote sensing. Thus, the TOPAZ simulation used here uses a hybrid approach, where Chl-a data are periodically assimilated from remote sensing-based measurements, reducing model uncertainty but affecting mass conservation. In addition to NPP and Chl-a concentration (Link D in Table 2), we also downloaded daily SIC (https://doi.org/10.48670/moi-00001) to evaluate against satellite records. An in-depth description and evaluation of TOPAZ model can be found in previous work (e.g., Schrum et al., 2006; Sakov et al., 2012; Daewel and Schrum, 2013; Yumruktepe et al., 2022).

BLING output refers to the ensemble output from 1980–2021 of three simulations of the coupled physical model (NEMO-LIM2) and biogeochemical model (BLINGv0DIC) run over overlapping periods and forced by a range of atmospheric conditions (Table 12). BLING model was initialized from climatology in 1958 which gives sufficient time for the surface ocean to spin-up. The ensemble output was chosen over individual output because it reduces the sensitivity of the model solution to atmospheric forcing and initial conditions. BLING model was chosen because it has the advantage of having a relatively low number of biogeochemical tracers (five compared to 12 in TOPAZ) allowing us to perform multiple long simulations at a relatively lower computational cost. Despite its lower complexity, BLING has shown good performance in the North Atlantic and Arctic (e.g., Galbraith et al., 2010, 2015; Castro de la Guardia et al., 2019; Deschepper et al., 2023). In addition to NPP and Chl-a, we also considered several physical variables (listed in Table 1) for the analysis of NPP drivers. An in-depth description and evaluation of BLING can be found in previous work (e.g., Galbraith et al., 2010, 2015; Castro de la Guardia, 2018).

The variables in the two models evolve according to the equations of state and mass conservation (e.g., Eq. (1)), but while the TOPAZ solution is relaxed to the observations with the aim of improving the solution, BLING is a fully prognostic model that does not assimilate the observations. The data assimilated by TOPAZ include SIC, ice thickness (iceH), sea surface temperature, sea level height, and surface Chl-a concentration (Sakov et al., 2012). Before its assimilation, the remote sensing-derived surface Chl-a concentrations are projected downward to 100 m assuming a Gaussian function (Uitz et al., 2006), similar to the approach used in the Takuvik NPP model. Another difference between the two models is that the phytoplankton biomass in BLING is not advected by ocean currents (e.g., the second term in Eq. (1) is null). Therefore, BLING represents only autochthonous production, which can be a limitation in areas with relatively strong ocean currents, such as in the north of Svalbard where biomass advection is suggested to increase the NPP by as much as 50% (Vernet et al., 2019). Meanwhile, TOPAZ is structurally limited in ice covered regions, because the physical model does not allow light penetration through the sea ice, thus preventing the growth of phytoplankton below the sea ice (Yumruktepe et al., 2022).

Both models use a representation of the same two phytoplankton groups, diatoms and flagellates, which are also responsible for most of the phytoplankton productivity and biomass in the NW-BS region (Rat'kova and Wassmann, 2002; Kohlbach et al., 2023a). Both models derive the NPP from the sum of the product of biomass and the productivity of each group. However, in BLING, NPP is limited by temperature, light, and Nutr, whereas in TOPAZ, NPP is only limited by light and Nutr.

2.4. Bioregionalization: K-mean clustering analysis

The goal of the bioregionalization analysis was to identify subregions with distinctly different phytoplankton phenological characteristics in NW-BS. K-mean clustering analysis is a statistically robust method that allows regionalization of gridded data products based on different spatial patterns in seasonality between grid cells. Bioregionalization analysis commonly uses Chl-a derived from remote sensing tools and normalized in space. The method has been successfully applied to identify drivers of the pelagic ecosystem in the Southern Ocean (Ardyna et al., 2017), the Labrador Sea (Marchese et al., 2019), the North Sea (Silva et al., 2021) and the eastern Pacific Ocean (Marchese et al., 2022). However, in NW-BS, remote sensing products have large temporal and spatial discontinuities due to sea ice and cloud cover (Fig. 2a,b). Therefore, we used simulated seasonal Chl-a climatology (1980–2021) from BLING averaged from depth 0–100 m to match the integration depth of the NPP analysis (noting that similar results were obtained if using 0–30 m layer).

The K-mean clustering analysis considers the Euclidean distance to form the clusters. We imposed a maximum of 40 clusters and 100 iterations. The best number of clusters was selected based on a silhouette score of at least 0.6, a minimal number of negative silhouette values, a similar number of grid points within each cluster, and following Ardyna et al. (2017) we also selected statistically different phytoplankton bloom parameters. Phytoplankton bloom parameters were defined using the BLING 5-day mean time series smoothed with a 10-day running mean (Silva et al., 2021). A grid cell was defined as having a phytoplankton bloom when the maximum Chl-a concentration was greater than 0.5 mg m^{-3} (Perrette et al., 2011; Silva et al., 2021). For grid cells with a phytoplankton bloom, we determined the peak day of the bloom as the day of maximum Chl-a concentration and estimated the seasonality of the bloom as the difference between the annual maximum and minimum Chl-a concentrations (Ardyna et al., 2017). Significance was evaluated using the Kruskal–Wallis H-test (H-test) and reported using the level of significance (p) and Chi-squared (χ^2) value with the groups' and error's degrees of freedom of the groups and the error (df) indicated as subscript and separated by a comma (that is, $\chi^2_{df1,df2}$).

Polygons were created for each cluster (subregion) and used to compute regional averages for each data and output source. In situ stations within each subregion were combined to obtain regional averages, assuming that the discrete station(s) was representative of the subregion. The Takuvik NPP was poorly available in the north (Fig. 3), so we assumed that the few available grid cells were representative of the northern region.

2.5. Data analysis

We cross-compared Chl-a, NPP, and SIC at each station using available estimates from in situ, remote sensing, and model outputs. A significant Pearson linear correlation was used to measure similarities between the output and the data. We considered significance as $p \leq 0.05$. For Chl-a cross-comparison purposes, we assumed that the MODIS-A Chl-a concentration approximated the values within the active mixing layer. The averaged active mixing layer is 30 m in the ice-covered region of the Barents Sea (Peralta-Ferriz and Woodgate, 2015) and along the Nansen Legacy station transect (ranging 10 – 50 m between March and September; Sandven et al., 2023). The mixing depth of 30 m was supported by regional observations of phytoplankton biomass concentrating in the upper 30 m of the water column (Reigstad et al., 2002), and approximate the averaged depth of the euphotic zone in the NW-BS region (28.5 m in Table 2 of Vernet et al., 1998). Therefore, Chl-a concentrations from other sources were averaged from 0 to 30 m depth.

The NPP from the in situ and the model output were interpolated from the surface to 100 m using 1 m bins, then integrated from the depth

of 0 to 100 m to match the processing of the Takuvik NPP data set. The depth of 100 m is a good choice for NPP because processes that affect phytoplankton, such as surface heating and mixing, can penetrate to almost 100 m (60–80 m) in the Barents Sea (Loeng, 1991; Wassmann et al., 2006a). The daily values of the NPP were integrated for each season and year. BLING 5-day mean NPP output was interpolated daily prior to temporal integration. Temporal interpolation was also necessary to fill the gaps in the seasonal climatology of the Takuvik output and in situ NPP data. We use the smoothing spline interpolation method (de Boor, 1978) when the grid cell/station had a fair amount of data before and after the maximum in the data (e.g., stations P1, P3, P5). However, when there were significant temporal gaps, this interpolation method was inadequate (e.g., stations P2, P4, P6, P7, SICE18, SICE19, PICE1). Thus, we develop a seasonal function for each grid cell using the BLING output (details in the Appendix Text A). The BLING seasonal function was used to interpolate when temporal gaps in remote sensing and in situ data were significant. BLING was chosen over TOPAZ due to its longer integration period and because it performed better in seasonal ice-covered regions due to the limitations related to under-ice blooms in the TOPAZ biogeochemical model (Yumruktepe et al., 2022).

The trends in the time series were calculated using linear regression and are reported with slope (b), and coefficient of determination (r^2). Interannual variability in time series from model output and remote sensing data was compared using the Pearson linear correlation coefficient (r) on the detrended time series (Mohamed et al., 2022a); note that the time series presented in the figures are non-detrended. We identified periods of significant change (e.g., regime change) in the time series using the MATLAB 2022b change point analysis package (Lavielle, 2005; Killick et al., 2012). We focus on mean statistics to find the most abrupt change in the time series using a minimum of 10 years between the change points. The significant difference between the medians of the two periods was then assessed and reported by the H-test.

Taking into account only the BLING output, normalized Principal Component Analysis (PCA) was used to identify patterns in the time series 1980–2021. Stepwise linear regression analysis was used to derive the most parsimonious model to predict the NPP. The input to the model included the physical variables listed in Table 1, and avoided multicollinearity by excluding predictor variables with a Variance Inflation Factor (VIF) > 10 following Goldsmit et al. (2021). Stepwise linear regression analysis used forward and backward iteration methods to include (or exclude) variables in (from) the model, based on the selection criterion of the adjusted r^2 improving by at least 0.1, while maintaining model significance. Highest adjusted-r^2 and lowest Root Mean Square Error (RMSE) identify the best models.

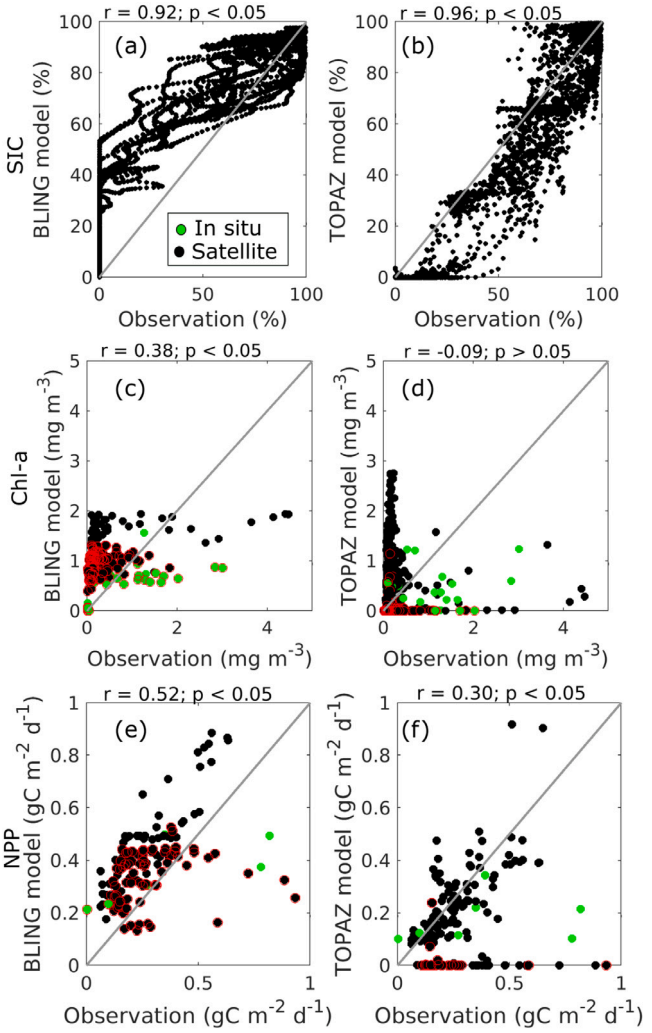

Fig. 4. Evaluation of BLING (a,c,e) and TOPAZ (b,d,f) model output versus remote sensing (black) and in situ data (green). Scatter plots of: (a–b) daily SIC from passive microwave sensors (1980–2021; Comiso, 2017), (c–d) daily Chl-a concentration averaged 0–30 m depth, and (e–f) daily NPP integrated 0–100 m depth. Displaying Pearson correlation coefficient r and significance level p between model output and observational data. Data points are classified as ice-free (no outline, modelled annual SIC < 50%) and ice-covered (red outline, modelled annual SIC > 50%). The diagonal grey line in a–f is the ideal 1 : 1 relationship between the model and the observations.

3. Results

3.1. Cross-evaluation of output and data

A comparison of the SIC output of the models with remote sensing data revealed that both BLING and TOPAZ had a good representation of the SIC with a high Pearson correlation ($r > 0.90$; Fig. 4a, b). Both models also captured the increase in SIC and shortening of open water seasons along the Nansen Legacy station transect with increasing latitude (Figure 1.5). In BLING sea ice melted later in spring and formed earlier in autumn, resulting in higher SIC (11 ± 2%) and longer ice-covered seasons relative to remote sensing data. However, the BLING SIC output from 1980 to 2021 captured the observed interannual variability of SIC in the NW-BS (Pearson correlation coefficient: $r = 0.8$, $p < 0.05$; Figure 1.2). The rate of SIC loss during the same period in BLING was 5% decade^{-1} (linear regression: $r^2 = 0.3$, $p < 0.05$), nearly identical to the remote sensing-derived estimate of 6% decade^{-1} (linear regression: $r^2 = 0.5$, $p < 0.05$; Figure 1.2).

A comparison of model Chl-a and NPP output with remote sensing and in situ data revealed a better overall representation of the data by the BLING model compared to the TOPAZ model in seasonally ice-covered waters (Fig. 4c–f). Chl-a was poorly represented by both models, both of which generally overestimated Chl-a concentration at low values and underestimated it at high values (Fig. 4c, d). However, large uncertainties arise from the Chl-a estimates, as there was also little agreement between Chl-a from MODIS-A and the in situ data ($r = 0.23$, $p > 0.05$).

NPP was much better represented by the two models, with a significant Pearson correlation between the output and data ($r = 0.52$ in BLING and $r = 0.30$ in TOPAZ; Fig. 4e, f). However, BLING consistently overestimated NPP in relation to observed data, and TOPAZ had a large underestimation error in ice-covered waters (e.g., red circles in Fig. 4a–d). The Pearson correlation between BLING output and data was higher if only in situ data was considered (Chl-a concentration: $r = 0.60$, $p < 0.05$; NPP: $r = 0.73$, $p < 0.05$). BLING captured some aspects of the seasonality of in situ NPP and Chl-a but overestimated its magnitude (Figures 1.3 and 1.4).

The modelled seasonality of the NPP and Chl-a concentrations at each station was difficult to cross-evaluate due to the large temporal

Table 3
Phytoplankton net primary production (NPP) in each subregion of the Northwestern Barents Sea (NW-BS). Regional mean of integrated annual and depth (0–100 m) NPP (**gC m^{-2} yr^{-1}**) with standard deviation, or range provided when available. Source data type numerical model (NM), remote sensing (RS). If the estimate is not available, it is marked as n.a.

Source	Type	Period	Atlantic	Subarctic	Arctic
BLING	NM	1980–2021	118 ± 30	82 ± 23	47 ± 12
TOPAZ	NM	2019–2021	45 ± 10	24 ± 3	10 ± 2
Takuvik	RS	2003–2011	78 ± 29	65 ± 15	18 ± 10
In situ	14C	2018, 2019	35 ± 14	43	37 ± 8
Literature[a]	NM/RS	1981–2011	107 ± 63	88 ± 17	41 ± 23
Reigstad et al. (2011)	NM	1995–2007	93–121	n.a.	50–60
Wassmann et al. (2006a,b)	NM	1981, 1984, 1998, 1999	120–160	75–100	40–60
Dalpadado et al. (2014)	RS	1998–2011	167	n.a.	44
Pabi et al. (2008)	RS	1998–2006	10–20	n.a.	1–10

[a] Mean does not consider outliers (more than 3 standard deviations from the mean).

gaps in the observed data (Figs. 2 and 3). Seasonal cycles were based on the climatology of the available periods in each data set. In TOPAZ the bloom was more abrupt and later relative to BLING, which better reflected the seasonality of remote sensing, particularly in the southern stations with more frequent data (Figures 1.3 and 1.4). The BLING model captured the length of the growing season in relation to the observations (Figures 1.3 and 1.4). However, the observed seasonality in the in situ data is skewed towards the model output as the snapshot measurements were extrapolated using the BLING seasonal function (Text A).

The seasonally integrated NPP of the model and the data (Fig. 5) suggest that summer was the period with the highest NPP (June–August, 74 ± 9% of the annual NPP), followed by spring (March–May, 13 ± 10% of the annual NPP), and autumn (September–November, 13 ± 7% of the annual NPP). Seasonally integrated NPP showed a strong latitudinal gradient with a higher NPP in the southern stations compared to the northern stations for the climatology estimates of BLING, TOPAZ, and Takuvik. In situ data showed that the NPP increased from P1 to P4 and then decreased towards the north. The in situ NPP estimates for the P4 station had an exceptionally high NPP. Comparing the annually integrated NPP between model output and observations (Fig. 5d), BLING climatology overestimated the annual NPP in almost all stations (BLING vs. Takuvik mean ± standard deviation: 21 ± 18 gC m^{-2} yr^{-1}; RMSE = 27; BLING vs. in situ: 27 ± 27 gC m^{-2} yr^{-1}; RMSE = 36.7), while the opposite was true for TOPAZ climatology (TOPAZ vs. Takuvik: −14 ± 12 gC m^{-2} yr^{-1}; RMSE = 18; TOPAZ vs. in situ: −11 ± 17 gC m^{-2} yr^{-1}; RMSE = 19).

3.2. NW-BS subregion NPP estimates and trends

The k-mean clustering analysis of the BLING Chl-a output suggested a division of NW-BS into three subregions (Fig. 6). We classified the subregions as Atlantic, Subarctic, and Arctic based on geographical area (Fig. 6a). Each subregion has unique seasonal cycles of Chl-a concentration (Fig. 6b) and significantly different phytoplankton bloom parameters (Fig. 6c–e; Table 13). The peak in Chl-a concentration was 10 and 30 days earlier in the Atlantic relative to the Subarctic and Arctic subregions, respectively. The annual mean Chl-a concentration in the Atlantic subregion was 30% and 50% higher than in the Subarctic and Arctic subregions, respectively. The seasonality of Chl-a concentration was highest in the Atlantic, followed by Subarctic and Arctic subregion.

The NPP regionally averaged and annually integrated followed a decreasing gradient from south to north, with the largest NPP in the Atlantic relative to the Subarctic and Arctic subregions based on the output of BLING and TOPAZ, Takuvik, and published values (Fig. 7; magnitudes in Table 3). Interestingly, in situ estimates did not reveal differences between subregions, however, they originated in two different years with strongly different environmental settings (Amargant-Arumi et al., 2023). For example, in situ estimates of the integrated NPP in the Atlantic subregion were 48.6 gC m^{-2} yr^{-1} in 2018 and 20.8 gC m^{-2} yr^{-1} in 2019. Also for the Arctic subregion, the NPP in 2018 (45.5 gC m^{-2} yr^{-1}) was higher than for 2019 (27.6 gC m^{-2} yr^{-1}). In the Subarctic subregion, the regional and annual NPP estimate was derived from a measurement in the late summer of 2019.

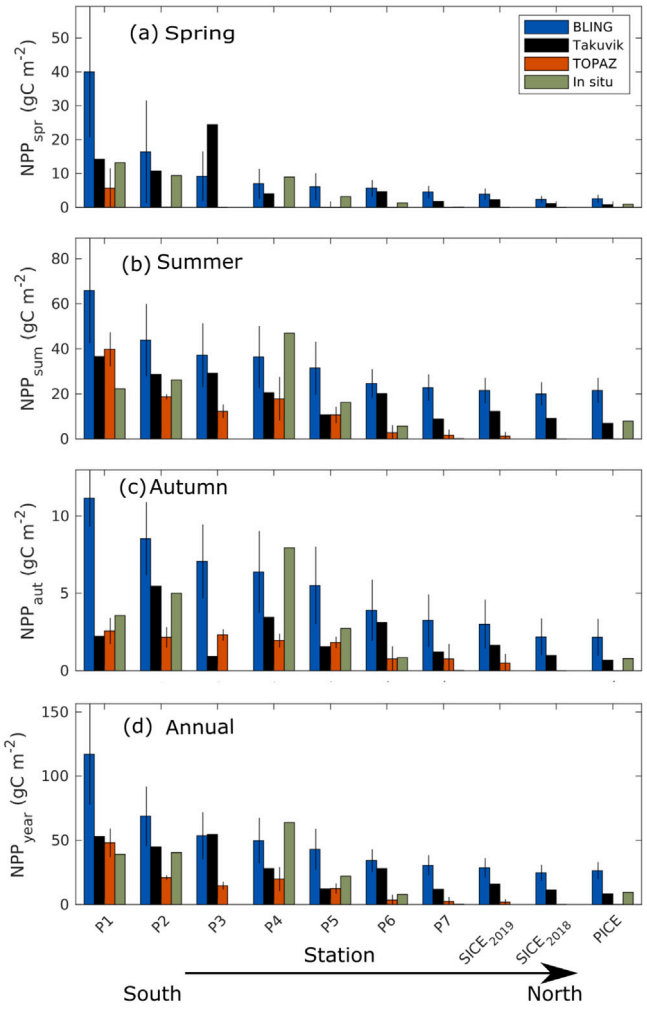

Fig. 5. Time and depth-integrated NPP at each station estimated by BLING (blue), Takuvik (black), TOPAZ (orange), and in situ (green). Depth integration (0–100 m). Temporal integration periods are (a) spring: March to May, (b) Summer: June to August, (c) Autumn: September to November, and (d) annual: January to December. Standard deviations are included when possible. For in situ and Takuvik the estimates are based on the fitted seasonal cycles (solid line in Figure 1.3). Note the different *y*-axis on each panel.

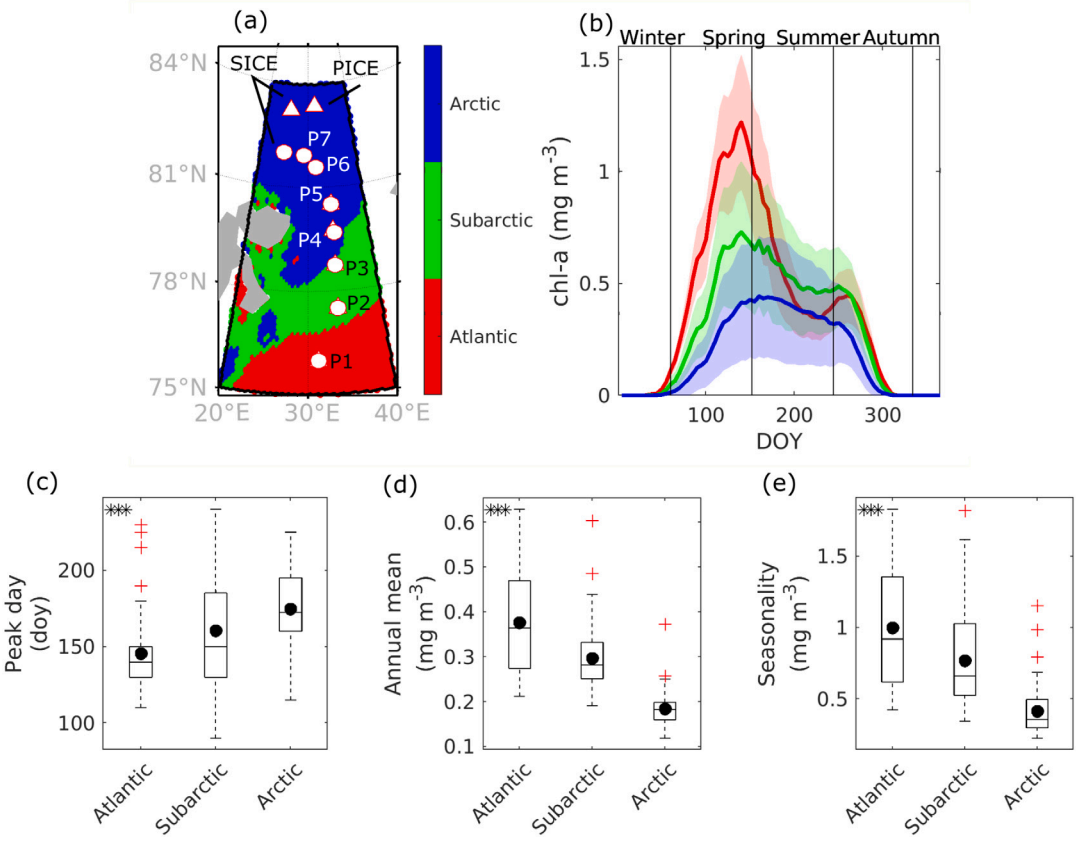

Fig. 6. Bioregionalization results for the NW-BS using BLING output. (a) Spatial pattern with symbols represent sampling stations as in Fig. 1. (b) Seasonal climatology of Chl-a in each subregion showing mean (solid line) and standard deviation (shading). Vertical black lines denote the temporal boundaries of the four seasons as defined in this study. (c–d) Parameters of the phytoplankton bloom: (c) Peak day, (d) annual mean, and (e) seasonality (annual maximum minus annual minimum). Black asterisk symbols in (c–d) indicate a significant difference between subregions (Table 13) and excluding outliers (red plus-symbols). The lower and upper edges of the box are the 25 and 75 percentiles, respectively. The error bars denote the maximum and minimum values. The middle lines denote the medians, and the black-filled circles denote the means.

The BLING and Takuvik estimates were closest to published values that were derived from a combination of output and remote sensing data (Table 3). Relative to published values, BLING overestimated the NPP in the Atlantic and Arctic subregions by 11 and 6 $gC\,m^{-2}\,yr^{-1}$, respectively, and underestimated it in the Subarctic subregion by 6 $gC\,m^{-2}\,yr^{-1}$. However, Takuvik and TOPAZ consistently underestimated the published values by approximately 25 and 50 $gC\,m^{-2}\,yr^{-1}$, respectively, in each subregion.

There were no long-term temporal trends in the annual NPP of BLING (1980–2021) or Takuvik (2003–2011) in any subregion. However, our analysis of BLING time series including NPP alongside the physical variables from Table 1, detected a change point in 2004 in the Atlantic subregion. The BLING time series showed a step increase in NPP in the Atlantic subregion in 2004, which coincided with a step decrease in SIC (Fig. 8). Between the two periods the NPP increased by 16% (median: $M_{80-03} = 111.2\,gC\,m^{-2}\,yr^{-1}$, $M_{04-21} = 132.4\,gC\,m^{-2}\,yr^{-1}$; H-test $\chi^2_{1,41} = 10.6$, $p < 0.01$), while the SIC decreased from a median of 39% before the regime shift to 11% after the regime shift (H-test $\chi^2_{1,41} = 24.6$, $p < 0.01$).

The BLING and Takuvik data sets had high interannual variability in the annual NPP (Fig. 8a–c). The interannual variability of BLING's time series was similar to that of the Takuvik data over the overlapping period (2003–2011) in the Arctic subregion, but not in the Atlantic or Subarctic subregion. This was confirmed by a high Pearson correlation between the time series of BLING and Takuvik NPP in the Arctic subregion ($r = 0.78$; $p < 0.05$), but low in the Atlantic ($r = -0.57$; $p = 0.11$) and Subarctic ($r = 0.27$; $p = 0.48$) subregions. Strong interannual variability driven by environmental settings was also evident in the in situ data (see above). The interannual variability of SIC (1980–2021)

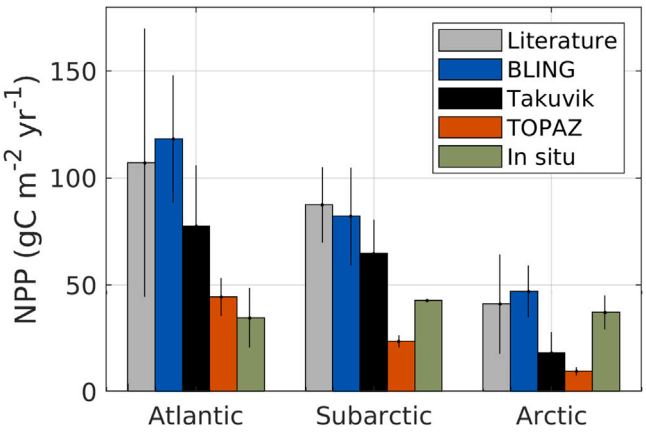

Fig. 7. Climatology of annual and depth-integrated (0–100 m) NPP in the NW-BS averaged over each subregions. Literature estimates combine remote sensing and model output and include different periods between 1981 to 2011 (sources listed in Table 3). The period considered in BLING 1980–2021, Takuvik 2003–2011, TOPAZ 2019–2021, in situ 2018–2019. For in situ and Takuvik the estimates are based on the fitted seasonal cycles from BLING (Text A). Values for NPP in Table 3.

in BLING followed that of remote sensing-derived SIC data in each subregion (Fig. 8d–f). The Pearson correlation for the detrended time series was high in the Atlantic ($r = 0.81$; $p < 0.05$), Subarctic ($r = 0.69$; $p < 0.05$), and Arctic subregions ($r = 0.68$; $p < 0.05$). BLING output also captured the observed rate of SIC loss between 1980 and 2021 in all subregions. BLING SIC decreased in the Atlantic subregion at a rate of

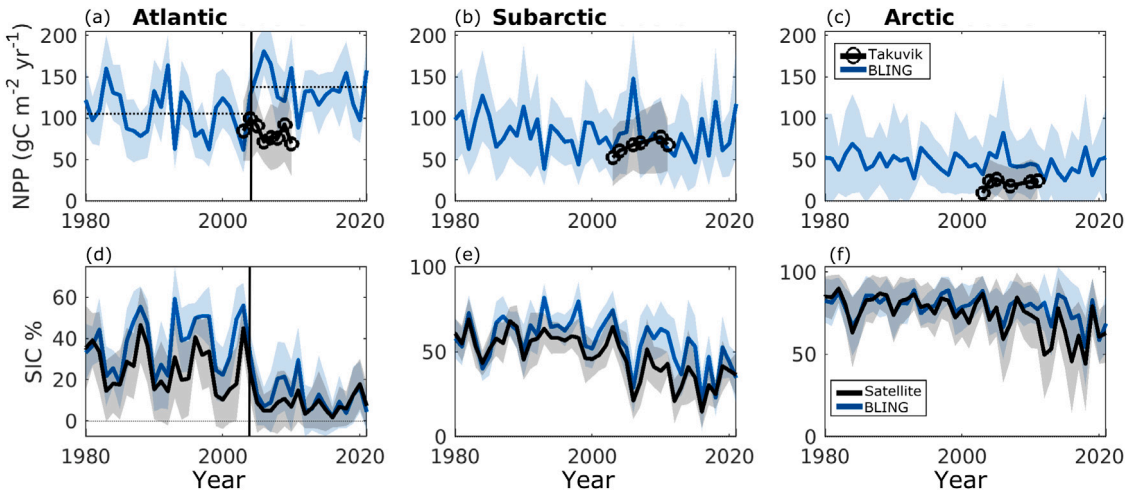

Fig. 8. Interannual variability of NPP and SIC on the three subregions of the NW-BS (solid line is the mean, shaded area is the standard deviation). In (a) and (d) vertical line marks an abrupt change in slope and mean of BLING NPP time series, and in (a) horizontal dotted lines are period mean.

$-8\%\,\text{decade}^{-1}$ ($r^2 = 0.4$; $p < 0.05$), in the Subarctic subregion at a rate of $-5\%\,\text{decade}^{-1}$ ($r^2 = 0.2$; $p < 0.05$) and in the Arctic subregion at a rate of $-2\%\,\text{decade}^{-1}$ ($r^2 = 0.1$; $p < 0.05$). Similarly, remote sensing SIC data suggest a rate of $-7\%\,\text{decade}^{-1}$ ($r^2 = 0.4$; $p < 0.05$) in the Atlantic and Subarctic subregions, and a rate of $-5\%\,\text{decade}^{-1}$ ($r^2 = 0.3$; $p < 0.05$) for the Arctic subregion.

The seasonal NPP estimated by the BLING output (Figure 1.7) suggested that in the three subregions, summer was the period of highest phytoplankton NPP, contributing $54 \pm 8\%$, $66 \pm 9\%$, and $73 \pm 5\%$ of the annual NPP in the Atlantic, Subarctic, and Arctic subregions, respectively. Spring was the second-highest contributing period with $35 \pm 6\%$, $22 \pm 8\%$, and $16 \pm 5\%$ of the annual NPP in the Atlantic, Subarctic, and Arctic subregions, respectively. The contribution was lowest in autumn (approximately $11 \pm 3\%$ in the three subregions) and almost null during winter (not shown).

In the Atlantic subregion, there was small positive trend in spring NPP (linear trend: $6.8\,\text{gC}\,\text{m}^{-2}\,\text{season}^{-1}\,\text{decade}^{-1}$, $r^2 = 0.2$, $p < 0.05$), driven by a step increase in spring NPP after 2004 (median: $M_{1980–2003} = 33.8\,\text{gC}\,\text{m}^{-2}\,\text{spring}^{-1}$, median: $M_{2004–2021} = 56.0\,\text{gC}\,\text{m}^{-2}\,\text{spring}^{-1}$; H-test $\chi^2_{1,41} = 17.8$, $p < 0.01$). In the Subarctic subregion, there was a small negative trend in summer ($6.3\,\text{gC}\,\text{m}^{-2}\,\text{season}^{-1}\,\text{decade}^{-1}$, $r^2 = 0.2$, $p < 0.05$) and autumn ($0.6\,\text{gC}\,\text{m}^{-2}\,\text{season}^{-1}\,\text{decade}^{-1}$, $r^2 = 0.1$, $p < 0.05$). In the Arctic subregion, there was a small negative trend in summer ($3.2\,\text{gC}\,\text{m}^{-2}\,\text{season}^{-1}\,\text{decade}^{-1}$, $r^2 = 0.2$, $p < 0.05$).

3.3. Physical drivers of NPP

A PCA and stepwise regression analysis were performed to identify the physical variables that accounted for most of the interannual variability in each subregion and season (Figs. 9–11). Principal Components (PC) 1 and 2 explained at least 50% of the interannual variability in the physical environment between years, and individually captured $42 \pm 13\%$ and $24 \pm 8\%$ of the variance, respectively. In the PC space of all subregions and seasons, we distinguish between the years before the simulated change point in the Atlantic subregion as triangles (1980–2003), and the years after the change point as circles (2004–2021). Consistently, years before the change point clustered closer together relative to the later period. In the PC space, the distance between points is analogous to the difference between individual years with respect to the variables considered. Thus, the two clusters indicated different environmental conditions before and after 2004, with years after 2004 having higher environmental heterogeneity.

AW and surface temperature (T) emerged as the dominant vectors along the direction of separation between the two periods clustered in every subregion and season. Therefore, these variables played a crucial role in distinguishing the two periods. The variables dominating the environmental heterogeneity within each period can be identified by having the largest vector along the direction of the spread of individual years within each cluster. SIC, T, and PAR emerged consistently as the dominant vectors along the direction of the spread of the triangles; therefore, these variables contributed the most to the environmental heterogeneity from 1980 to 2003. The number of days with light (Lys) and surface Nutr concentration consistently emerged as the largest vectors along the direction of the spread of the circles, indicating that these variables contributed the most to the environmental heterogeneity from 2004 to 2021.

Additionally, the colour of the symbols within the PC space served to highlight the differences in NPP between years (warmer colour indicating higher NPP). In the Atlantic subregion, in particular, the annual, spring, and summer panels (Fig. 9a–c) showed that years after 2004 had higher NPP compared to years before 2004. SIC, iceH, PAR, AW volume and T emerged as the dominant vectors along the direction of the NPP gradient, suggesting that these contributed more significantly to the differences in NPP between the two periods. SIC, iceH vectors oppose the gradient of the NPP thus their association with NPP was negative, while PAR, AW volume, and T vectors follow the gradient of the NPP thus their association was positive.

Stepwise linear regression allowed us to isolate the best set of NPP predictors for each subregion and season Table 1, but excluding variables with a high colinearity index allowed us to isolate the best set of NPP predictors for each subregion and season (Table 4). The best predictor of annual NPP in the Atlantic subregion was the depth of the maximum mixing layer, MXD (positive association), while in the Subarctic and Arctic subregions, PAR and Nutr (positive association). The best predictor of spring NPP in the three subregions was PAR (positive association). However, none of the variables considered could achieve a good level of predictability of the NPP in autumn and summer in the Atlantic subregion (for example, the models are not significant or had low adjusted r^2). The summer NPP in the Subarctic subregion was best predicted by the number of open water days with light (OWL; positive association) and the volume of AW (negative association), while the autumn NPP was best predicted by MXD (positive association). Summer NPP in the Arctic subregion was best predicted by OWL (positive association) and snow depth (snowH; negative association), while the autumn NPP was best predicted by PAR and MXD (positive association).

These NPP models highlighted the general importance of multiple factors, and the timing of these factors, for positive changes in NPP throughout the NW-BS. The absence of SIC as a predictor of NPP

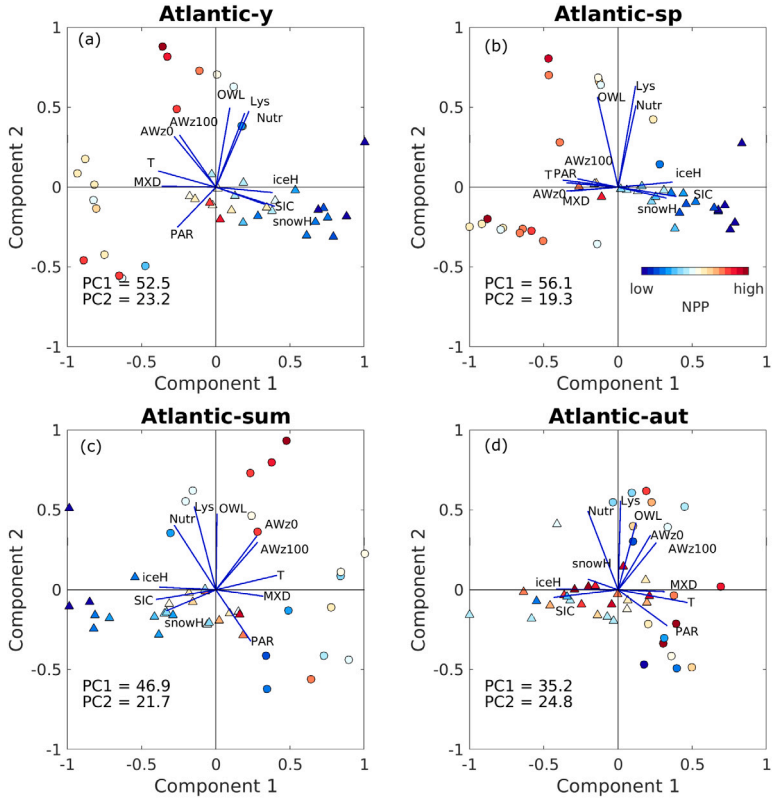

Fig. 9. Principal component analysis (PCA) of environmental variability in the Atlantic subregion of the NW-BS considering four seasons (a) annual, (b) spring, (c) summer, and (d) autumn. Symbols indicate years before 2004 (triangles) and after 2004, inclusive (circles). The colour within each symbol is the normalized NPP [range 0–1]. The PCA considered the standardized physical variables from BLING output as listed in Table 1.The variance explained by the first two principal components is given in the bottom left of each panel.

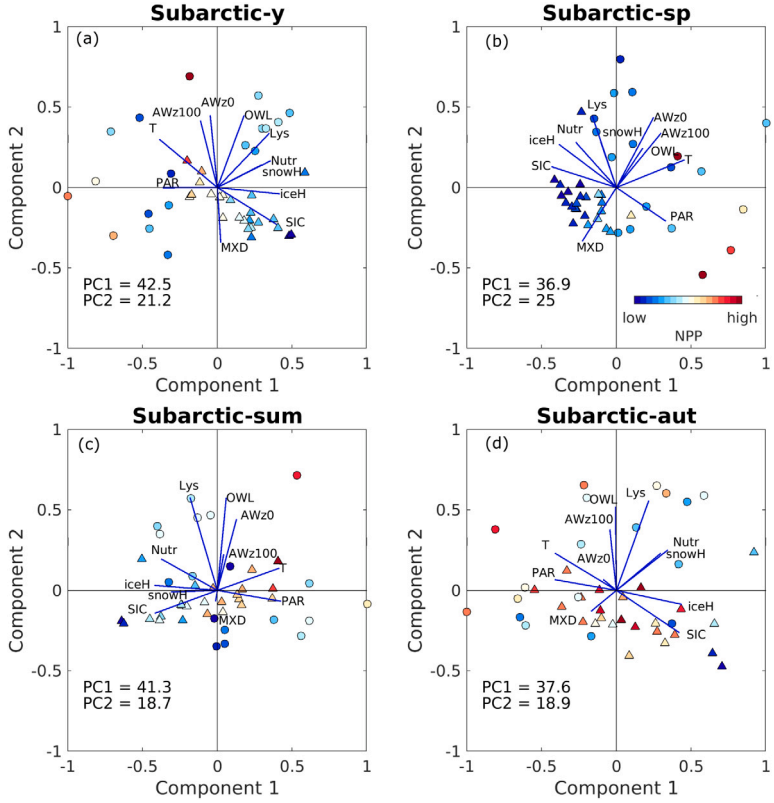

Fig. 10. Same as Fig. 9 but for the Subarctic subregion.

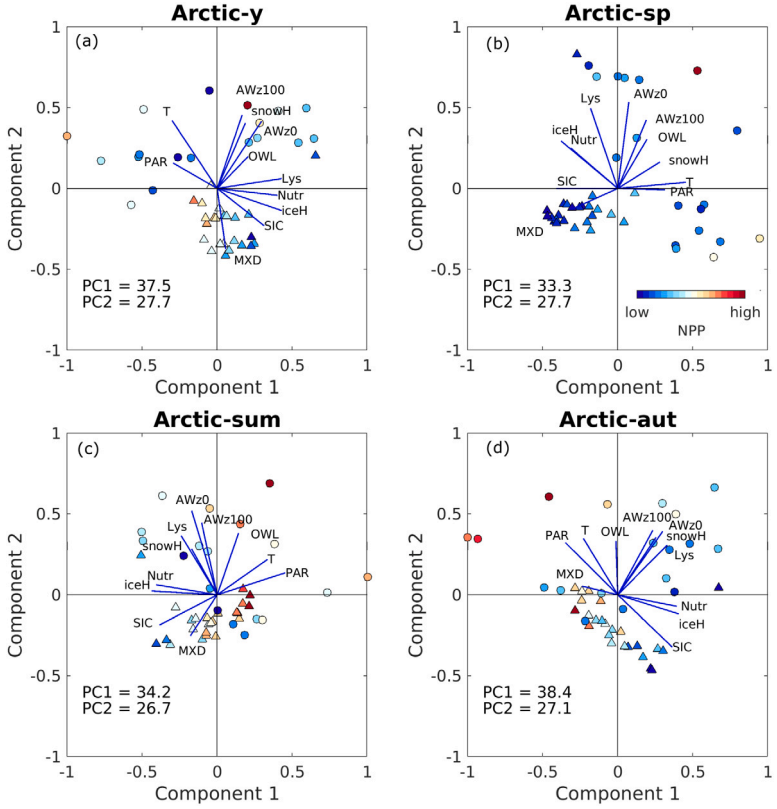

Fig. 11. Same as Fig. 9 but for the Arctic subregion.

Table 4
Stepwise linear models to predict NPP from selected variables[a] in each season and subregion of NW-BS.

Model	Equation	Adjusted r^2	RMSE[b]
Atlantic annual	NPP = 28.2 + 0.6 × MXD	0.46	22.2
Atlantic spring	NPP = −5.3 + 66 × PAR	0.90	5.69
Atlantic summer	NPP = 70 − 357 × snowH	0.25	13.5
Atlantic autumn	Not significant		
Subarctic annual	NPP = −64.8 + 190.4 × Nutr + 51.7 × PAR	0.64	13.9
Subarctic spring	NPP = −3.0 + 54.4 × PAR	0.88	3.97
Subarctic summer	NPP = 41.9 + 2.8 × OWL − 0.1 × AWz0 − 0.01 × AWz100	0.46	11.9
Subarctic autumn	NPP = 3.4 + 0.1 × MXD	0.43	1.52
Arctic annual	NPP = 41.4 + 394 × PAR × Nutr	0.76	6.04
Arctic spring	NPP = −6.1 + 64.0 × PAR	0.86	1.35
Arctic summer	NPP = 31.6 + 4.8 × OWL − 156 × snowH	0.46	6.79
Arctic autumn	NPP = 10.0 + 0.01 × MXD + 12.8 × PAR	0.73	0.84

[a] Variables' definition and units are listed in Table 1.
[b] RMSE abbreviation stands for Root Mean Squared Error.

was surprising. However, this variable had a high colinearity index, which led to its exclusion as a predictor variable. SIC was negatively correlated with PAR and maximum mixing layer depth (MXD), which are variables selected within the stepwise linear models presented in Table 4.

4. Discussion

4.1. Limitations of the datasets

The data sets used here have limitations regarding their temporal resolution, methodology, and assumptions (Table 5). These limitations are a source of uncertainties and are the main reasons for the differences in the quantitative estimates of NPP and Chl-a presented in Table 3 and Figs. 4, 5 and 7. There is greater certainty in the qualitative aspects of the results than in absolute values, since seasonal and regional patterns, such as seasonality and bioregionalization analysis, show convergence into distinct patterns (e.g., Fig. 6, 1.3–1.5). In this sense, the cross-comparison of the four data sets with published estimates was essential to highlight the limitations and advantages of each data set within the NW-BS. We start our discussion by addressing how limitations can affect results and propose ways in which we may reduce their impact in future studies.

4.1.1. The need for more frequent sampling

The poor availability of in situ data in NW-BS, combined with temporal and spatial variability, limits, at various levels, the use of single data sources as reference points. However, in situ data are often used as a reference to evaluate the range of magnitude and seasonality of variables from other data and output sources. We found that extrapolation of available in situ data (one observation per year per station) was not sufficient to resolve the observed seasonal variability (Reigstad et al., 2002; Matrai et al., 2007), and due to the methodology used

Table 5
Summary of limitation of the data sources.

Dataset	Type	Sources of uncertainties
BLING	NM	(1) no advection of biomass; (2) convert biomass to carbon using a fixed carbon to phosphate ratio of 106; (3) derived Chl-a from biomass as a function of light and iron concentration; (4) derive NPP from biomass; (5) the biological model depends on the representation of physics.
TOPAZ[a]	NM	(1) no biomass under sea ice; (2) Chl-a is derived from carbon (biomass) as a function of light and Nutr; (4) assimilation of Chl-a using a Gaussian function to extrapolate from the surface to 100 m; (5) NPP is not temperature limited; (6) the biological model depends on the representation of physics.
Takuvik	RM	(1) space and time gaps; (2) use a Gaussian function to extrapolate Chl-a from the surface to 100 m; (3) convert Chl-a to carbon using a fixed carbon to Chl-a ratio of 90; (4) derive NPP from Chl-a; (5) NPP is not temperature limited.
In situ	14C	(1) space and time gaps; (2) may include the impact of transient events, such as storms.

[a] TOPAZ is coupled with ECOSMO biogeochemical model.

here, it was biased towards the seasonality of the BLING model (details in Text A). However, the integrated annual NPP derived from this extrapolation was consistent with other data sources in this study, except for station P4 (Fig. 5). The relatively high NPP of this station disrupted the gradual increase in NPP from south to north, which contrasted with the results of other data presented in this study and published elsewhere (e.g., Wassmann et al., 2006a; Pabi et al., 2008; Reigstad et al., 2011; Arrigo et al., 2011).

In general, the in situ NPP was at the low end of the estimated range (Fig. 5 and Table 3). However, based on measurements from 2018 and 2019, in situ NPP may represent extremes of the climatology state, while the NPP estimated by the other data sources are averaged over longer periods and thus may be more representative of the climatology state. Alternatively, the low annual NPP of the in situ data could be explained by the fact that the NPP was limited in Nutr at the time of sampling (summer) and therefore carried the limitation of Nutr to the annual estimate. Previous work has suggested that low phytoplankton production can be explained by a stronger Nutr limitation (Matrai et al., 2007), which may be associated with the retreat of sea ice creating oligotrophic conditions in summer (Kohlbach et al., 2023a). Furthermore, we found that the annual in situ NPP in 2018 was higher than in 2019, yet Amargant-Arumi et al. (2023) suggests that the two years had similar production in summer. Thus, the Nutr-limited summer measurements do not reflect the annual behaviour of NPP, and may not be sufficient to derive the annual estimates that were, in the context of this paper, used to evaluate the magnitude of data/output coming from other sources.

Clearly, seasonal in situ sampling including spring, summer, and autumn is required to estimate annual new/regenerated production (albeit still limited by spatial restrictions). We recommend spring and summer should be high-priority periods for field sampling, as they have the highest contribution to the annual NPP (Fig. 5). Interannual variability in the duration and timing of phytoplankton blooms may remain an inherent challenge in field sampling. For example, the difference of 10 to 30 days in the timing of the bloom between the ice-free region (Atlantic subregion) and the ice-covered regions (Subarctic and Arctic subregions; Fig. 6c) will likely cause logistical problems in the planning of field campaigns. This strong latitudinal gradient in the timing of the bloom corroborates the observations in 1999 (Matrai et al., 2007).

Additionally, individual weather patterns, cloudiness, mixing, Nutr upwelling, development of zooplankton, etc., will still impact the in situ measured values. This, highlighting the value of using models to extend and contrast from the single-day in situ measurement to seasonal and interannual patterns as done in this study. We suggest that novel in situ measurement approaches using profiling floats should be used here to achieve daily estimates of NPP over complete seasons throughout the region (Stoer and Fennel, 2023).

4.1.2. Significant gaps in the remote sensing coverage

Gaps in the Takuvik NPP output highlighted the regional limitation of remote sensing products in NW-BS due to the high cloud cover and sea ice. Therefore, we cannot recommend them to investigate the seasonal or temporal dynamics of phytoplankton in the NW-BS. Alternatively, the gaps could be filled using trained algorithms (e.g., Bélanger et al., 2013; Dalpadado et al., 2014; Arrigo and van Dijken, 2015), but not without creating uncertainties in trends (Babin et al., 2015). Remote sensing data had low NPP values in the Arctic subregion, but this was biased by the lack of data due to the presence of sea ice. In addition, the vertical extrapolation of surface Chl-a to depth 100 m used by remote sensing to calculate NPP has a tendency to underestimate NPP in waters with a sub-surface Chl-a maximum (Lee et al., 2015); which is a typical feature of our study region (Sandven et al., 2023). In the near future, remote sensing data sets could be complemented with data from ARGO float (see above), moorings, and autonomous underwater vehicles to form a 3D view of the ocean that could help close the gaps and increase the certainty of remote sensing NPP estimates and data assimilation models like TOPAZ.

4.1.3. Structural differences: Chl-a/biomass ratios, sea ice, and biomass advection

The differences between the NPP and Chl-a in the output of the model, remote sensing and in situ data may be due to the selection of photosynthetic parameters and stoichiometry (Schrum et al., 2006). In particular, uncertainties are associated with the variability of Chl-a/biomass ratios. Remote sensing and in situ data calculate the Chl-a concentration from ocean colour, observed fluorescence of in situ fluorometers, or during expeditions using fluorometric determination of Chl-a in filtered seawater samples. However, remote sensing and in situ data calculate NPP using a fixed Chl-a to carbon ratio, which can lead to inaccuracies in annual integrated NPP estimates because this ratio is a function of light and Nutr (e.g.; Cloern et al., 1995; Burt et al., 2018). Meanwhile, the models derive Chl-a and NPP from biomass, which has a layer of uncertainty related to errors in the model's representation of ocean physics. The models derive Chl-a concentration taking into account the variable Chl-a to carbon ratio as a function of Nutr and light limitation. However, this can also introduce errors in the Chl-a estimates, which may explain its poorer cross-comparison relative to NPP (Fig. 4c–f).

Uncertainties in the biomass estimates of these coupled ocean-biogeochemical models are also sensitive to the representation of ocean physics, particularly sea ice and mixing (Mousing et al., 2023), and structural differences between the two models associated with the calculations of advection and turbulent exchanges and in biogeochemical gains and losses. TOPAZ assimilates some of the ocean's physical and biological properties, leading to a relatively good comparison with remote sensing NPP in the ice-free region (Fig. 4). However, TOPAZ underestimated the NPP in seasonally ice-covered regions due to a lack of light under sea ice, resulting in zero NPP under sea ice. This highlighted the advantage of assimilating observed ocean properties, but also the significant structural limitation of assuming zero biomass under sea ice. Field observations in NW-BS noted phytoplankton in the pre-bloom stage under sea ice (Rat'kova and Wassmann, 2002), with a biomass of 20 $gC\ m^{-2}$ under SIC of 20 and 80% (Reigstad et al., 2002). Elsewhere in ice-covered waters, large phytoplankton blooms have been observed to develop at very low light levels below the pack ice (e.g., Assmy et al., 2017; Søgaard et al., 2021). Such blooms may occur as early as the onset of sea ice melt and extend to open water in the late spring (Ardyna et al., 2020) and can draw down Nutr before the

area becomes ice-free and detectable by satellites (Arrigo et al., 2017; Ardyna et al., 2020). In fact, PAR under sea ice can be substantially more than previously considered (Pavlov et al., 2017), and especially high under new sea ice with a thin snow cover (Kauko et al., 2017). Improving the representation of light under sea ice will most likely improve TOPAZ's NPP estimates in the Arctic subregions.

BLING incorporates a representation of light transmission through sea ice and enables productivity beneath the ice. However, there is a delayed melting of sea ice in BLING (Figure 1.5) that may be partially responsible for a seasonal delay in the peak of NPP. In BLING the phytoplankton bloom peaked in late May to mid-June, while field studies suggest that the peak in productivity occurs in spring (mid-May) after the retreat of sea ice (Vernet et al., 1998; Matrai et al., 2007). Measurements in the south of NW-BS in 1999 showed that phytoplankton production followed the retreating edge of the ice, with the peak day in May at 75°N, and later in July at 77°N (Rat'kova and Wassmann, 2002; Matrai et al., 2007). Thus, we cannot rule out that the later bloom in BLING may also be an artefact of regional averaging over large latitudinal ranges (e.g., Atlantic subregion latitudinal range is 75–77.5°N). Another important structural difference is that the BLING model does not consider advection phytoplankton. Vernet et al. (2019) demonstrated the importance of advected biomass in NPP along current pathways of the AW and suggested that the peak of autochthonous production was June (which is similar to BLING). Thus, the delayed seasonal cycle in BLING could also be a result of not representing phytoplankton advection. This seasonal delay in BLING may also explain why the period with the highest integrated productivity in the three subregions was summer (June–August) instead of spring (March–May). Despite the structural limitations mentioned, the annual climatology of the BLING NPP was closer to the published values in the three subregions than the other data and output used in this study (e.g., Fig. 6 Wassmann et al., 2006a; Pabi et al., 2008; Reigstad et al., 2011; Dalpadado et al., 2014).

4.1.4. Advection of biomass and npp north of svalbard

The stations (P6–P7) were located within the main AW advection pathway north of Svalbard (Lind and Ingvaldsen, 2012; Koenig et al., 2016; Lundesgaard et al., 2022; Koenig et al., 2023). The relatively shallow depth of AW along the continental slope north of Svalbard facilitates the transfer of its properties (e.g., Nutr, biomass and heat) to surface waters (Koenig et al., 2016, 2017). Model sensitivity experiments (Vernet et al., 2019) recently demonstrated that biomass advection can significantly enhance NPP along the shelf break north of Svalbard, where these stations were located. However, we found no evidence of enhanced NPP at these northern stations compared to the other stations along the south-to-north transect in any of our data sets (Fig. 5).

A plausible explanation for the inability to properly resolve advection in this region could be the poor seasonal and spatial coverage of in situ and remote sensing (which also affects the TOPAZ model), whereas BLING is inheritable limited as it does not advect biomass. Furthermore, the strong presence of sea ice at these northernmost stations would not allow for increases in phytoplankton NPP, prior to the in situ sampling, again pointing towards a delay in the phytoplankton bloom timing with increasing latitude. In situ Chl-a concentration, which had more frequent sampling, showed a local increase in biomass at stations P4–P7 (Figures 1.4 and 1.6). The advection of biomass and Nutr in AW has been suggested to explain the regionally higher concentration of Chl-a, particularly at station P6 (Kohlbach et al., 2023a; Koenig et al., 2023; Kohler et al., 2023). In support of this, other studies have also observed high zooplankton biomass at station P6 supported by advective biomass (Wold et al., 2023).

4.1.5. NPP estimates do not include ice algae NPP

The estimates of NPP presented in this study do not include the contribution of ice algae or the competition for Nutr between phytoplankton and ice algae, although both groups are abundant in the ice covered regions of the Barents Sea (Hegseth and von Quillfeldt, 2022). The NPP of ice algae has previously been estimated at between 16 and 22% of total NPP in the ice-covered regions of the Barents Sea (Hegseth, 1998), but the exact contribution of ice algae is probably sensitive to the type, age, and thickness of sea ice (Hegseth and von Quillfeldt, 2022). The suggested range agrees well with observations from other Arctic regions: 3–25% on the Arctic shelves (Legendre et al., 1992; Michel et al., 1993; Gosselin et al., 1997), up to 57% in the permanently ice covered central Arctic Ocean (Gosselin et al., 1997) and 30–40% in the seasonally ice covered region of the Canadian Arctic based on model output (Silva et al., 2021). One future direction would be to include estimates of the contribution of ice algae to NW-BS and quantify the combined long-term trends of ice algae and phytoplankton NPP jointly. Based on previous work (Wassmann et al., 2006a), we expect the contribution of ice algae (autochthonous or allochthonous) to be small and obviously spatially limited to the northern parts of the study area.

4.2. Bioregions confirmed the strong link with the physical environment

Our bioregionalization of NW-BS using simulated phytoplankton biomass for the period 1980–2021 identified three subregions: (1) an Atlantic subregion with a major bloom peak in spring and a smaller bloom peak in autumn, (2) a Subarctic subregion with only one distinct bloom in spring, and (3) an Arctic subregion with only a summer bloom that was less intense than in the other subregions. The use of phytoplankton biomass for the regionalization analysis was novel, but the resulting three subregions support the three main GPP domains suggested by Wassmann et al. (2010) and Wassmann (2011). Similarly to these authors, we found (i) a high NPP subregion in the ice-free area (Atlantic subregion), (ii) a moderate NPP subregion in the seasonal ice-covered area (Subarctic subregion), and (iii) a low NPP subregion in the permanently ice-covered area (Arctic subregion).

Our three subregions also have differences in the physical environment; for example, from south to north, the annual mean SIC increases, the AW volume decreases, T cools, MXD shoals, and PAR decreases. The boundaries of the subregions largely follow the distribution of AW, ArW and SIC (Ingvaldsen and Loeng, 2009; Wassmann et al., 2010). Thus, it is not surprising, that the resulting three subregions support previous subdivisions based on distinct physical features, such as sea surface temperature (Rey, 1991), dominant water masses (Dalpadado et al., 2014), and sea ice conditions (Mohamed et al., 2022a). All of these studies confirmed the strong link between the dynamics of high-latitude phytoplankton and the physical environment (Ådlandsvik and Loeng, 1991; Wassmann et al., 2006a; Lind and Ingvaldsen, 2012; Koul et al., 2022).

The estimates of NPP for each subregion were constrained by the combination of model output and observational data; which was particularly important given the limitations of the data sets. Taking into account the range in annual NPP estimates (Table 3), we were able to show an overall negative gradient from the Atlantic to the Arctic subregion, which corroborates previously published work from models and in situ observations (Wassmann et al., 2006a; Pabi et al., 2008; Reigstad et al., 2011; Dalpadado et al., 2014; Arrigo et al., 2011). The higher NPP in the southern relative to the northern Barents Sea has been associated with a higher Nutr, higher PAR, and lower sea ice in the southern areas relative to the northern areas (Rey, 1991; Reigstad et al., 2002, 2011).

4.3. Step change increase in autochthonous NPP

The BLING output suggests that after 2004 the environmental heterogeneity increased throughout the NW-BS and was accompanied by a step increase in NPP in the Atlantic subregion that parallelled a decrease in SIC in the same subregion. In the BLING simulation, the volume of AW in the three subregions increased between 2003 and 2015 and could be responsible for the simulated step change in SIC and NPP in 2004 in the Atlantic subregion. A different coupled physical–biogeochemical model (1966–2015) also showed an increase in AW influx into the southern Barents Sea between 2001 and 2010, and identified it as the main driver of the sudden decrease in SIC that led to a regional increase in NPP (Koul et al., 2022). Our interpretation of the step increase in NPP, thus follows the previously noted coupling of high interannual and decadal variability of NPP and physical environment, especially the influx of AW and SIC (Wassmann et al., 2006a; Koul et al., 2022). However, in the Subarctic and Arctic Subregions there was no parallel increase in NPP even when SIC also decreased. This could be partially explained by the shoaling trends in MXD and lower surface Nutr in these subregions that opposed the deepening of MXD in the Atlantic subregion. Slagstad et al. (2015) showed that NPP may not increase if increasing AW and decreasing SIC combine with stronger stratification and lower Nutr replenishment to surface water.

The absence of clear temporal trends in annual NPP for our study area in the BLING output (1980–2021) and Takuvik data (2003–2011) contrasts with published studies using remote sensing data that suggested that NPP in the Barents Sea increased by 5, 28 and 88%yr^{-1} for the periods 1998–2010, 1998–2012, 1998–2018, respectively (Bélanger et al., 2013; Arrigo and van Dijken, 2015; Lewis et al., 2020). However, this comparison is biased as the other studies filled the spatial and temporal gaps in the remote sensing data, in contrast to the Takuvik data we used (e.g., Fig. 3), thus, adding a layer of uncertainty to the trends (Babin et al., 2015) that could explain the wide range of NPP trends estimated by these studies. Additionally, the published positive trends in NPP considered the whole Barents Sea and could thus be driven by the disproportional increase in NPP in near-coastal waters and the northeastern Barents Sea (NE-BS) (Bélanger et al., 2013; Arrigo and van Dijken, 2015; Lewis et al., 2020). These other regions have a stronger influence of river runoff and inflowing AW which can fuel the NPP by increasing Nutr (Dalpadado et al., 2014; Koul et al., 2022; Frey et al., 2022). Meanwhile, in NW-BS, the stronger influence of Nutr-poor ArW makes NPP less likely to respond positively to loss of SIC and increase in PAR compared to NE-BS (Slagstad et al., 2015). NPP in NW-BS is also less sensitive to atmospheric warming (e.g., Slagstad et al., 2011, 2015). It should also be noted that the loss of sea ice and thus the increase in light availability for phytoplankton growth has been lower in the NW-BS relative to the NE-BS (e.g., Arrigo and van Dijken, 2015; Mohamed et al., 2022a), most likely because the strong topographic steering of the polar front in the NW-BS sends most of the warm AW to the NE-BS (Oziel et al., 2020).

Increasing the concentration of Nutr is hypothesized to drive the more recent increase in NPP throughout the Arctic Ocean (Arrigo and van Dijken, 2015; Lewis et al., 2020). However, our BLING simulation indicates that Nutr increased from 1980 to 2010 but decreased thereafter in the NW-BS, which could be a major reason explaining our observed absence of positive trends in NPP and the seasonal declines in NPP in the Subarctic and Arctic subregions. Rey (2012) and Hátún et al. (2017) also found a declining Nutr in AW entering the southern Barents Sea (1990–2013) and linked it to decadal changes in the depth of deep convection in the western subpolar gyre. However, in the European sector of the Arctic and north of Svalbard, including our Arctic subregion, a data compilation from 1980 to 2016 found no evidence of decreasing Nutr in the AW (Duarte et al., 2021). Therefore, it is unclear what drives the decreasing concentration of Nutr in the BLING output, but the simulation results suggest that it could be linked to phenological changes in NPP and connectivity between subregions: the positive trend in spring NPP in the Atlantic subregion could imply that the peak productivity is shifting from summer to spring as sea ice decreases in the model; thus, Nutr-depleted waters are advected north, causing the negative trend in summer and in autumn NPP in the Subarctic and Arctic subregions.

Alternatively, the allochthonous influx of biomass is also hypothesized to be positively associated with the increase in NPP throughout the Arctic in remote sensing (Arrigo and van Dijken, 2015; Lewis et al., 2020). Using a model simulation Vernet et al. (2019) suggested that allochthonous biomass is responsible for more than 50% of the gross primary production along the main current pathways of AW north of Svalbard. The advection of biomass in the AW current (and thus allochthonous production) is significantly lower within the interior NW-BS compared to the north of Svalbard and NE-BS (Vernet et al., 2019; Oziel et al., 2020). The BLING model does not resolve the advection of phytoplankton or zooplankton; hence, the absence of positive NPP trends in BLING could support the hypothesis that the allochthonous influx of biomass drives the recent increase in NPP, particularly in the north of the domain.

4.4. Physical drivers of simulated NPP

The NPP drivers varied between the subregions and seasons (Table 4), but PAR and MXD were the most important predictor variables. Other predictors, such as OWL, AW volume, and Nutr, were seasonally and/or regionally important. Field observations and other model outputs have suggested a strong correlation between SIC and NPP (Wassmann et al., 2006a; Matrai et al., 2007; Koul et al., 2022). However, in the present study, SIC was excluded from most stepwise regression models due to its high correlation with other predictor variables; however, this does not imply that there is no association between SIC and NPP (which is apparent in Fig. 8). The role of SIC is inherently included in variables like PAR, which is directly dependent on the presence of ice and the associated snow cover.

We found that the simulated annual NPP in the Atlantic subregion was best predicted by MXD (positive association) and in the Subarctic and Arctic by Nutr and PAR (positive associations). The overwhelming importance of MXD in the Atlantic subregion supports previous research that identified deepening MXD as one of the main drivers of increased NPP by increasing Nutr in the southern Barents Sea and the Arctic Shelf Seas (Wassmann et al., 2006a; Slagstad et al., 2015; Silva et al., 2021). In the Arctic and Subarctic subregions, BLING corroborates the hypothesis that Nutr and PAR have a decisive role in explaining the interannual variability of NPP (Arrigo and van Dijken, 2015; Lewis et al., 2020). The seasonal drivers of NPP varied, but during the highly productive season, summer, NPP responded positively to increasing OWL in the Subarctic and Arctic subregions, and negatively to increasing AW volume and snowH in the Subarctic and Arctic subregions, respectively. Positive responses to OWL and negative responses to snowH can be explained by the direct relationship between these variables and PAR (Leu et al., 2015). Meanwhile, the negative response of NPP to the volume of AW contradicts the general view that the presence of AW increases the amount of NPP in the Barents Sea (Koul et al., 2022). However, in these two subregions, MXD shoaled in summer at the same time that AW volume increased, suggesting a strengthening stratification that can negatively affect NPP by reducing Nutr resupply to surface water (Slagstad et al., 2015).

NPP forms the base of the pelagic marine food web and can be linked to the energy transferred to higher trophic levels and to the corresponding production of harvestable resources (Ottersen and Stenseth, 2001). Thus, as the regional environment becomes more heterogeneous year-to-year, it raises questions about the implications for the regional ecosystem. The linear models for NPP presented in Table 4 in addition to identifying the main drivers of the simulated NPP, could be used as a first approach to estimate the response of the pelagic ecosystem when the NPP data are unavailable.

4.5. Contribution of NW-BS to norwegian fisheries

NW-BS is an important fishing ground for commercial harvested fish stocks, including herring (*Clupea harengus*), Atlantic cod (*Gadus morhua*), capelin (*Mallotus villosus*), saithe (*Polliachus virens*) and haddock (*Melanogrammus aeglefinus*) (e.g., Gjøsæter, 2009). Fish are highly dependent on secondary production (e.g., zooplankton), and may also feed on smaller fish and benthic invertebrates. However, seasonal zooplankton growth is closely coupled with the phytoplankton NPP in the NW-BS (Kohlbach et al., 2023b). Thus, in an exercise to determine the importance of NW-BS for Norwegian fisheries, we upscaled the phytoplankton NPP for the NW-BS area (Fig. 1) and compared it with the primary production required (PPR, sensu Pauly and Christensen, 1995) to sustain the yields (Y) of some of the main fish species via the food web. PPR can be estimated using the equation: $PPR = Y/(0.1^{TL-1})$; where TL stands for trophic level and 0.1 is the assumed energy transfer efficiency.

We calculate the PPR (Table 14) for Atlantic cod, haddock, and saithe using TL values reported in the Fishbase (https://www.fishbase.se, the Norwegian fish database) and approximate values for Y of some of the main commercial species reported in the last 10 years in the Norwegian Fisheries Directorate (Fiskeridirektoratet, 2021). We estimate a PPR of 90 $TgC\,yr^{-1}$ to support the yields of these three species within the broad Atlantic–Arctic Ocean (between 30–60°E and 62–80°N; Figure 1.8). Arrigo and van Dijken (2015) estimated the total NPP of 130 $TgC\,yr^{-1}$ over approximately the same broad area. Taking into account the model and observations of this study, we estimate that the total NPP in NW-BS ranges from 15 to 48 ×, $TgC\,yr^{-1}$, which is within the same order of magnitude as the PPR in the broad area of the Atlantic–Arctic Ocean. The results suggest that the current fish catch depends on a significant fraction (approximately 1/3) of the NPP in the NW-BS, implying that changes in NPP could directly affect the marine harvest.

With this exercise, we highlight the importance of NPP in NW-BS for Norwegian fisheries, bringing attention to the importance of properly matching geographical and temporal NPP estimates with fishing yields towards sustainable management of marine resources. Considering that we did not include other important fishing resources, such as herring and capelin, it is rather likely that a much larger fraction of NPP is required to sustain the Norwegian fisheries' harvest, leading to considerable pressure on the marine ecosystem. Any future trends on autochthonous and allochthonous NPP should be incorporated into fisheries management to help adjust fishing yields and redirect efforts to different trophic levels to keep PPR under controlled levels. Therefore, improving the methods used to estimate and upgrade NPP to different fishing areas, including modelling tools, is of utmost importance to the sustainable management of the Barents Sea marine ecosystem.

4.6. Conclusion

We highlight the complexity of estimating annual and seasonal NPP in the NW-BS using different tools. Although NPP is a key measure of ecosystem performance and an indicator of the impacts of climate change the absence of reliable ground-truth data hampers an accurate assessment of its magnitude. Models are practical for NPP estimation and trend analysis, however, they again need reliable data for evaluation. Therefore, we suggest that more efforts are needed to merge model outputs with observations and to compare the various estimation methods to refine NPP assessments.

The three delineated regions based on the phytoplankton phenology within the NW-BS highlighted the intimate connection between the abiotic and biotic components of the ecosystem. The spatial diversity of these subregions yields distinct physical drivers of NPP in seasons and spaces. In particular, although we did not detect an increase in annual NPP in response to substantial sea ice loss in the three regions, either from remote sensing or simulation, after 2004 the simulation witnessed a regime change with increased interannual heterogeneity in the physical environment. Further analysis could shed light on the events that led to the regime change and its influence on NPP.

Our study brings to light the substantial contribution of the NW-BS region to locally harvested fish resources despite its relatively small size. Therefore, we cannot overstate the importance of continuing efforts to predict and understand these ecologically important metrics, annual and seasonal NPP.

CRediT authorship contribution statement

Laura Castro de la Guardia: Conception and design of study, Analysis and/or interpretation of data, Writing – original draft, Writing – review & editing. **Tania Hernández Fariñas:** Conception and design of study, Analysis and/or interpretation of data, Writing – review & editing. **Christian Marchese:** Conception and design of study, Analysis and/or interpretation of data, Writing – review & editing. **Martí Amargant-Arumí:** Acquisition of data and output, Analysis and/or interpretation of data, Writing – review & editing. **Paul G. Myers:** Acquisition of data and output, Analysis and/or interpretation of data, Writing – review & editing. **Simon Bélanger:** Acquisition of data and output, Analysis and/or interpretation of data, Writing – review & editing. **Philipp Assmy:** Conception and design of study, Acquisition of data and output, Analysis and/or interpretation of data, Writing – review & editing. **Rolf Gradinger:** Conception and design of study, Acquisition of data and output, Analysis and/or interpretation of data, Writing – review & editing. **Pedro Duarte:** Conception and design of study, Analysis and/or interpretation of data, Writing – original draft, Writing – review & editing.

Declaration of competing interest

The authors declare that they have no known competing financial interests or personal relationships that could have appeared to influence the work reported in this paper.

Data availability

The following data sets were used in this study:

- Polygon of subregions provided as csv file as supporting material attached to this paper.
- In situ chl-a data in Table 11 and https://doi.org/10.21335/NMDC-1371694848.
- In situ NPP data Table 11.
- MODIS-A chlorophyll-a data (DOI: 10.5067/AQUA/MODIS/L3M/CHL/2022).
- Percent sea ice and cloud cover fraction (https://hermes.acri.fr/index.php?class=archive).
- SIC derived from remote sensing (https://doi.org/10.5067/7Q8HCCWS4I0R).
- TOPAZ output for NPP and Chl-a concentration (https://doi.org/10.48670/moi-00003).
- TOPAZ output for SIC (https://doi.org/10.48670/moi-00001).
- BLING model output (http://knossos.eas.ualberta.ca/anha/model.php) and contact Paul G. Myers (pmyers@ualberta.ca).

Acknowledgements

We acknowledge the excellent support received by the crew of RV Kronprins Haakon and the participating scientists of the Nansen Legacy field expeditions. The authors are grateful to the NEMO development team and the Drakkar project for providing the model and continuous guidance, the efforts of NASA Goddard Space Flight Center, Ocean Ecology Laboratory, the Ocean Biology Processing Group for maintaining Chl-A and SIC data sets, the Takuvik Research Laboratory based at the University of Laval for making available and maintaining the Takuvik

NPP data, the Digital Research Alliance of Canada, Westgrid and Compute Canada (https://alliancecan.ca/en) and the Norwegian Research Infrastructure Services (NRIS) and Sigma2 (https://www.sigma2.no/) for computational resources to perform our analysis, simulations, and archival of model experiments. Special thanks to Tobias Vonnahme for conducting the 2018 NPP assessments onboard RV Kronprins Haakon, and to colleagues Melissa Chierici and Elizabeth Jones at the Institute of Marine Research, Norway and Agneta Fransson at the Norwegian Polar Institute, Tromsø for their support with the laboratory analysis. All authors approved the version of the manuscript to be published.

Funding information

This study was supported by the Research Council of Norway through the project *The Nansen Legacy* [*RCN* #276730]. Further funding was provided by the Norwegian Metacenter for Computational Science application *NN9300K – Ecosystem modelling of the Arctic Ocean around Svalbard*.

Appendix A. Supplementary data

Supplementary material related to this article can be found online at https://doi.org/10.1016/j.pocean.2023.103160.

References

Ådlandsvik, B., Loeng, H., 1991. A study of the climatic system in the Barents Sea. Polar Res. 10, 45–50. http://dx.doi.org/10.3402/polar.v10i1.6726.

Amargant-Arumi, M., Müller, O., et al., 2023. Interannual differences in sea ice regime in the north-western Barents Sea cause major changes in summer pelagic production and export mechanisms. Prog. Oceanogr. (in press).

Ardyna, M., Babin, M., Gosselin, M., Devred, E., Bélanger, S., Matsuoka, A., Tremblay, J.-E., 2013. Parameterization of vertical chlorophyll a in the Arctic Ocean: impact of the subsurface chlorophyll maximum on regional, seasonal, and annual primary production estimates. Biogeosciences 10, 4383–4404. http://dx.doi.org/10.5194/bg-10-4383-2013.

Ardyna, M., Claustre, H., Sallée, J.-B., D'Ovidio, F., Gentili, B., van Dijken, G., D'Ortenzio, F., Arrigo, K.R., 2017. Delineating environmental control of phytoplankton biomass and phenology in the Southern Ocean. Geophys. Res. Lett. 44, 5016–5024. http://dx.doi.org/10.1002/2016GL072428.

Ardyna, M., Mundy, C.J., Mayot, N., Matthes, L.C., Oziel, L., Horvat, C., Leu, E., Assmy, P., Hill, V., Matrai, P.A., Gale, M., Melnikov, I.A., Arrigo, K.R., 2020. Under-ice phytoplankton blooms: Shedding light on the invisible part of arctic primary production. Front. Mar. Sci. 7, http://dx.doi.org/10.3389/fmars.2020.608032.

Arrigo, K.R., Matrai, P.A., van Dijken, G.L., 2011. Primary productivity in the Arctic Ocean: Impacts of complex optical properties and subsurface chlorophyll maxima on large-scale estimates. J. Geophys. Res.: Oceans 116, http://dx.doi.org/10.1029/2011JC007273.

Arrigo, K.R., Mills, M.M., van Dijken, G.L., Lowry, K.E., Pickart, R.S., Schlitzer, R., 2017. Late spring nitrate distributions beneath the ice-covered northeastern chukchi shelf. J. Geophys. Res.: Biogeosci. 122, 2409–2417. http://dx.doi.org/10.1002/2017JG003881.

Arrigo, K.R., van Dijken, G.L., 2015. Continued increases in Arctic Ocean primary production. Prog. Oceanogr. 136, 60–70. http://dx.doi.org/10.1016/j.pocean.2015.05.002, synthesis of Arctic Research (SOAR).

Assmy, P., Fernández-Méndez, M., Duarte, P., Meyer, A., Randelhoff, A., Mundy, C.J., Olsen, L.M., Kauko, H.M., Bailey, A., Chierici, M., Cohen, L., Doulgeris, A.P., Ehn, J.K., Fransson, A., Gerland, S., Hop, H., Hudson, S.R., Hughes, N., Itkin, P., Johnsen, G., King, J.A., Koch, B.P., Koenig, Z., Kwasniewski, S., Laney, S.R., Nicolaus, M., Pavlov, A.K., Polashenski, C.M., Provost, C., Rösel, A., Sandbu, M., Spreen, G., Smedsrud, L.H., Sundfjord, A., Taskjelle, T., Tatarek, A., Wiktor, J., Wagner, P.M., Wold, A., Steen, H., Granskog, M.A., 2017. Leads in Arctic pack ice enable early phytoplankton blooms below snow-covered sea ice. Sci. Rep. 7, 40850. http://dx.doi.org/10.1038/srep40850.

Babin, M., Bélanger, S., Ellingsen, I., Forest, A., Le Fouest, V., Lacour, T., Ardyna, M., Slagstad, D., 2015. Estimation of primary production in the Arctic Ocean using ocean colour remote sensing and coupled physical–biological models: Strengths, limitations and how they compare. Prog. Oceanogr. 139, 197–220. http://dx.doi.org/10.1016/j.pocean.2015.08.008, overarching perspectives of contemporary and future ecosystems in the Arctic Ocean.

Basedow, S.L., Zhou, M., Tande, K.S., 2014. Secondary production at the Polar Front, Barents Sea 2007. J. Mar. Syst. 130, 147–159. http://dx.doi.org/10.1016/j.jmarsys.2013.07.015.

Bélanger, S., Babin, M., Tremblay, J.-E., 2013. Increasing cloudiness in Arctic damps the increase in phytoplankton primary production due to sea ice receding. Biogeosciences 10, 4087–4101. http://dx.doi.org/10.5194/bg-10-4087-2013.

Burt, W.J., Westberry, T.K., Behrenfeld, M.J., Zeng, C., Izett, R.W., Tortell, P.D., 2018. Carbon: Chlorophyll ratios and net primary productivity of Subarctic Pacific surface waters derived from autonomous shipboard sensors. Glob. Biogeochem. Cycles 32, 267–288. http://dx.doi.org/10.1002/2017GB005783.

Castro de la Guardia, L., 2018. Modelling the Response of Arctic and Subarctic Marine Systems To Climate Warming (Ph.D. thesis). University of Alberta, Edmonton, Canada, http://dx.doi.org/10.7939/R31G0J98H.

Castro de la Guardia, L., Garcia-Quintana, Y., Claret, M., Hu, X., Galbraith, E.D., Myers, P.G., 2019. Assessing the role of high-frequency winds and sea ice loss on arctic phytoplankton blooms in an ice-ocean-biogeochemical model. J. Geophys. Res.: Biogeosci. 124, 2728–2750. http://dx.doi.org/10.1029/2018JG004869.

Cloern, J.E., Grenz, C., Vidergar-Lucas, L., 1995. An empirical model of the phytoplankton chlorophyll : carbon ratio-the conversion factor between productivity and growth rate. Limnol. Oceanogr. 40, 1313–1321. http://dx.doi.org/10.4319/lo.1995.40.7.1313.

Comiso, J.C., 2017. Bootstrap sea ice concentrations from Nimbus-7 SMMR and DMSP SSM/ISSMIS, version 3. [1980–2021]. http://dx.doi.org/10.5067/7Q8HCCWS4I0R, [accessed: 2022].

Daewel, U., Schrum, C., 2013. Simulating long-term dynamics of the coupled North Sea and Baltic Sea ecosystem with ECOSMO II: Model description and validation. J. Mar. Syst. 119–120, 30–49. http://dx.doi.org/10.1016/j.jmarsys.2013.03.008.

Dalpadado, P., Arrigo, K.R., Hjøllo, S.S., Rey, F., Ingvaldsen, R.B., Sperfeld, E., van Dijken, G.L., Stige, L.C., Olsen, A., Ottersen, G., 2014. Productivity in the Barents Sea - Response to recent climate variability. PLOS ONE 9, 1–15. http://dx.doi.org/10.1371/journal.pone.0095273.

de Boor, C.A., 1978. Practical guide to splines. In: Applied Mathematical Sciences. Springer, New York, NY.

Deschepper, I., Myers, P.G., Lavoie, D., Papakyriakou, T., Maps, F., 2023. Understanding the physical forcings behind the biogeochemical productivity of the Hudson Bay Complex. J. Geophys. Res.: Biogeosci. 128, e2022JG007294. http://dx.doi.org/10.1029/2022JG007294, e2022JG007294 2022JG007294.

Duarte, P., Meyer, A., Moreau, S., 2021. Nutrients in water masses in the Atlantic Sector of the Arctic Ocean: Temporal trends, mixing and links with primary production. J. Geophys. Res.: Oceans 126, e2021JC017413. http://dx.doi.org/10.1029/2021JC017413, e2021JC017413 2021JC017413.

Efstathiou, E., Eldevik, T., Årthun, M., Lind, S., 2022. Spatial patterns, mechanisms, and predictability of Barents Sea ice change. J. Clim. 35, 2961–2973. http://dx.doi.org/10.1175/JCLI-D-21-0044.1.

Fiskeridirektoratet, 2021. Economic and Biological Figures from Norwegian Fisheries 2021. Tech. Rep. 2464-3157, Fiskeridirektoratet, Norway, Statistikk, https://www.fiskeridir.no/English/Fisheries/Statistics/Economic-and-biological-key-figures/.

Frey, K.E., Comiso, J.C., Cooper, L.W., Garcia-Eidell, C., Grebmeier, J.M., Stock, L.V., 2022. Arctic Ocean Primary Productivity: The Response of Marine Algae To Climate Warming and Sea Ice Decline. Tech. Rep. 48682, National Oceanic and Atmospheric Administration. Office of Oceanic and Atmospheric Research, United States, http://dx.doi.org/10.25923/0je1-te61, NOAA Arctic Report Card Series.

Galbraith, E.D., Gnanadesikan, A., Dunne, J.P., Hiscock, M.R., 2010. Regional impacts of iron-light colimitation in a global biogeochemical model. Biogeosciences 7, 1043–1064. http://dx.doi.org/10.5194/bg-7-1043-2010.

Galbraith, E.D., Kwon, E.Y., Bianchi, D., Hain, M.P., Sarmiento, J.L., 2015. The impact of atmospheric pCO2 on carbon isotope ratios of the atmosphere and ocean. Glob. Biogeochem. Cycles 29, 307–324. http://dx.doi.org/10.1002/2014GB004929.

Gjøsæter, H., 2009. Commercial fisheries (fish, seafood and marine mammals). In: Skshaug, E., Johnsen, G., Kovacs, K. (Eds.), Ecosystem Barents Sea. Tapir Academic Press, Cambridge, United Kingdom and New York, NY, USA, pp. 373–414, book chapter 16, https://www.researchgate.net/publication/283899239_Commercial_fisheries_fish_seafood_and_marine_mammals.

Goldsmit, J., Schlegel, R.W., Filbee-Dexter, K., MacGregor, K.A., Johnson, L.E., Mundy, C.J., Savoie, A.M., McKindsey, C.W., Howland, .K.L., Archambault, P., 2021. Kelp in the eastern Canadian arctic: Current and future predictions of habitat suitability and cover. Front. Mar. Sci. 8, http://dx.doi.org/10.3389/fmars.2021.742209.

Gosselin, M., Levasseur, M., Wheeler, P.A., Horner, R.A., Booth, B.C., 1997. New measurements of phytoplankton and ice algal production in the Arctic Ocean. Deep Sea Res. Part II 44, 1623–1644. http://dx.doi.org/10.1016/S0967-0645(97)00054-4.

Hátún, H., Azetsu-Scott, K., Somavilla, R., Rey, F., Johnson, C., Mathis, M., Mikolajewicz, U., Coupel, P., Tremblay, J.-E., Hartman, S., Pacariz, S.V., Salter, I., Ólafsson, J., 2017. The subpolar gyre regulates silicate concentrations in the North Atlantic. Sci. Rep. 7, 14576. http://dx.doi.org/10.1038/s41598-017-14837-4.

Hegseth, E.N., 1998. Primary production of the northern Barents Sea. Polar Res. 17, 113–123. http://dx.doi.org/10.3402/polar.v17i2.6611.

Hegseth, E.N., von Quillfeldt, C., 2022. The sub-ice algal communities of the Barents Sea pack ice: Temporal and spatial distribution of biomass and species. J. Mar. Sci. Eng. 10, http://dx.doi.org/10.3390/jmse10020164.

Hu, C., Lee, Z., Franz, B., 2012. Chlorophyll-a algorithms for oligotrophic oceans: A novel approach based on three–band reflectance difference. J. Geophys. Res.: Oceans 117, http://dx.doi.org/10.1029/2011JC007395.

Huot, Y., Babin, M., Bruyant, F., 2013. Photosynthetic parameters in the Beaufort Sea in relation to the phytoplankton community structure. Biogeosciences 10, 3445–3454. http://dx.doi.org/10.5194/bg-10-3445-2013.

Ingvaldsen, R.B., Loeng, H., 2009. Physical oceanography. In: Skshaug, E., Johnsen, G., Kovacs, K. (Eds.), Ecosystem Barents Sea. Tapir Academic Press, Cambridge, United Kingdom and New York, NY, USA, pp. 33–64, book chapter 2.

Isaksen, K., Nordli, Ø., Ivanov, B., Køltzow, M.A.Ø., Aaboe, S., Gjelten, H.M., Mezghani, A., Eastwood, S., Førland, E., Benestad, R.E., Hanssen-Bauer, I., Brækkan, R., Sviashchennikov, P., Demin, V., Revina, A., Karandasheva, T., 2022. Exceptional warming over the Barents area. Sci. Rep. 12, 9371. http://dx.doi.org/10.1038/s41598-022-13568-5.

Kauko, H.M., Taskjelle, T., Assmy, P., Pavlov, A.K., Mundy, C.J., Duarte, P., Fernández-Méndez, M., Olsen, L.M., Hudson, S.R., Johnsen, G., Elliott, A., Wang, F., Granskog, M.A., 2017. Windows in Arctic sea ice: Light transmission and ice algae in a refrozen lead. J. Geophys. Res.: Biogeosci. 122, 1486–1505. http://dx.doi.org/10.1002/2016JG003626.

Killick, R., Fearnhead, P., Eckley, I.A., 2012. Optimal detection of changepoints with a linear computational cost. J. Amer. Statist. Assoc. 107, 1590–1598. http://dx.doi.org/10.1080/01621459.2012.737745.

Koenig, Z., Lind, S., Lundesgaar, O., Muilwijk, M., Sandven, H., Assmy, P., Assmann, K., Chierici, M., Fransson, A., Gerland, S., Jones, E., Renner, A.H.H., Granskog, M.A., 2023. From winter to late summer in the northwestern Barents Sea Shelf: Sea ice and upper ocean evolution and impacts on nutrient and phytoplankton dynamics. Prog. Oceanogr. In revision.

Koenig, Z., Provost, C., Villacieros-Robineau, N., Sennéchael, N., Meyer, A., 2016. Winter ocean-ice interactions under thin sea ice observed by IAOOS platforms during N-ICE2015: Salty surface mixed layer and active basal melt. J. Geophys. Res.: Oceans 121, 7898–7916. http://dx.doi.org/10.1002/2016JC012195.

Koenig, Z., Provost, C., Villacieros-Robineau, N., Sennéchael, N., Meyer, A., Lellouche, J.-M., Garric, G., 2017. Atlantic waters inflow north of Svalbard: Insights from IAOOS observations and Mercator Ocean global operational system during N-ICE2015. J. Geophys. Res.: Oceans 122, 1254–1273. http://dx.doi.org/10.1002/2016JC012424.

Kohlbach, D., Goraguer, L., Bodur, Y.V., Müller, O., Amargant-Arumí, M., Blix, K., Bratbak, G., Chierici, M., Dąbrowska, A.M., Dietrich, U., Edvardsen, B., García, L.M., Gradinger, R., Hop, H., Jones, E., Lundesgaard, Øyvind, Olsen, L.M., Reigstad, M., Saubrekka, K., Tatarek, A., Wiktor, J.M., Wold, A., Assmy, P., 2023a. Earlier sea-ice melt extends the oligotrophic summer period in the Barents Sea with low algal biomass and associated low vertical flux. Prog. Oceanogr. 213, 103018. http://dx.doi.org/10.1016/j.pocean.2023.103018.

Kohlbach, D., Lebreton, B., Guillou, G., Wold, A., Hop, H., Graeve, M., Assmy, P., 2023b. Dependency of Arctic zooplankton on pelagic food sources: New insights from fatty acid and stable isotope analyses. Limnol. Oceanogr. http://dx.doi.org/10.1002/lno.12423, n/a.

Kohler, S.G., Heimburger-Boavida, L.-E., Assmy, P., Oliver Muller, S.T., Digernes, M.G., Ndungu, K., Ardelan, M.V., 2023. Biotic transformation of methylmercury at the onset of the Arctic spring bloom. Prog. Oceanogr. In revision.

Kortsch, S., Primicerio, R., Aschan, M., Lind, S., Dolgov, A.V., Planque, B., 2019. Food-web structure varies along environmental gradients in a high-latitude marine ecosystem. Ecography 42, 295–308. http://dx.doi.org/10.1111/ecog.03443.

Koul, V., Brune, S., Baehr, J., Schrum, C., 2022. Impact of decadal trends in the surface climate of the north atlantic subpolar gyre on the marine environment of the barents sea. Front. Mar. Sci. 8, http://dx.doi.org/10.3389/fmars.2021.778335.

Lavielle, M., 2005. Using penalized contrasts for the change-point problem. Signal Process. 85, 1501–1510. http://dx.doi.org/10.1016/j.sigpro.2005.01.012.

Lee, Y.J., Matrai, P.A., Friedrichs, M.A.M., Saba, V.S., Antoine, D., Ardyna, M., Asanuma, I., Babin, M., Bélanger, S., Benoît-Gagné, M., Devred, E., Fernández-Méndez, M., Gentili, B., Hirawake, T., Kang, S.-H., Kameda, T., Katlein, C., Lee, S.H., Lee, Z., Mélin, F., Scardi, M., Smyth, T.J., Tang, S., Turpie, K.R., Waters, K.J., Westberry, T.K., 2015. An assessment of phytoplankton primary productivity in the arctic ocean from satellite ocean color/in situ chlorophyll-a based models. J. Geophys. Res.: Oceans 120, 6508–6541. http://dx.doi.org/10.1002/2015JC011018.

Legendre, L., Ackley, S.F., Dieckmann, G.S., Gulliksen, B., Horner, R., Hoshiai, T., Melnikov, I.A., Reeburgh, W.S., Spindler, M., Sullivan, C.W., 1992. Ecology of sea ice biota. Polar Biol. 12, 429–444. http://dx.doi.org/10.1007/BF00243114.

Leu, E., Mundy, C., Assmy, P., Campbell, K., Gabrielsen, T., Gosselin, M., Juul-Pedersen, T., Gradinger, R., 2015. Arctic spring awakening – Steering principles behind the phenology of vernal ice algal blooms. Prog. Oceanogr. 139, 151–170. http://dx.doi.org/10.1016/j.pocean.2015.07.012.

Lewis, K.M., van Dijken, G.L., Arrigo, K.R., 2020. Changes in phytoplankton concentration now drive increased Arctic Ocean primary production. Science 369, 198–202. http://dx.doi.org/10.1126/science.aay8380.

Lind, S., Ingvaldsen, R.B., 2012. Variability and impacts of Atlantic Water entering the Barents Sea from the north. Deep Sea Res. Part I 62, 70–88. http://dx.doi.org/10.1016/j.dsr.2011.12.007.

Loeng, H., 1991. Features of the physical oceanographic conditions of the Barents Sea. Polar Res. 10, 5–18. http://dx.doi.org/10.3402/polar.v10i1.6723.

Lundesgaard, Ø., Sundfjord, A., Lind, S., Nilsen, F., Renner, A.H.H., 2022. Import of Atlantic Water and sea ice controls the ocean environment in the northern Barents Sea. Ocean Sci. 18, 1389–1418. http://dx.doi.org/10.5194/os-18-1389-2022.

Marchese, C., Albouy, C., Tremblay, J.-É., Dumont, D., D'Ortenzio, F., Vissault, S., Bélanger, S., 2017. Changes in phytoplankton bloom phenology over the North Water (NOW) polynya: a response to changing environmental conditions. Polar Biol. 40, 1721–1737. http://dx.doi.org/10.1007/s00300-017-2095-2.

Marchese, C., Castro de la Guardia, L., Myers, P.G., Bélanger, S., 2019. Regional differences and inter-annual variability in the timing of surface phytoplankton blooms in the Labrador Sea. Ecol. Indic. 96, 81–90. http://dx.doi.org/10.1016/j.ecolind.2018.08.053.

Marchese, C., Hunt, B.P.V., Giannini, F., Ehrler, M., Costa, M., 2022. Bioregionalization of the coastal and open oceans of British Columbia and Southeast Alaska based on Sentinel-3A satellite-derived phytoplankton seasonality. Front. Mar. Sci. 9, http://dx.doi.org/10.3389/fmars.2022.968470.

Matrai, P., Vernet, M., Wassmann, P., 2007. Relating temporal and spatial patterns of DMSP in the Barents Sea to phytoplankton biomass and productivity. J. Mar. Syst. 67, 83–101. http://dx.doi.org/10.1016/j.jmarsys.2006.10.001.

Mayot, N., Matrai, P.A., Arjona, A., Bélanger, S., Marchese, C., Jaegler, T., Ardyna, M., Steele, M., 2020. Springtime export of arctic sea ice influences phytoplankton production in the greenland sea. J. Geophys. Res.: Oceans 125, e2019JC015799. http://dx.doi.org/10.1029/2019JC015799.

Michel, C., Legendre, L., Therriault, J.-C., Demers, S., Vandevelde, T., 1993. Springtime coupling between ice algal and phytoplankton assemblages in southeastern Hudson Bay, Canadian Arctic. Polar Biol. 13, 429–444. http://dx.doi.org/10.1007/BF00233135.

Mohamed, B., Nilsen, F., Skogseth, R., 2022a. Interannual and decadal variability of sea surface temperature and sea ice concentration in the Barents Sea. Remote Sens. 14, http://dx.doi.org/10.3390/rs14174413.

Mohamed, B., Nilsen, F., Skogseth, R., 2022b. Marine heatwaves characteristics in the barents sea based on high resolution satellite data (1982–2020). Front. Mar. Sci. 9, http://dx.doi.org/10.3389/fmars.2022.821646.

Mousing, E.A., Ellingen, I., Hjøllo, S.S., Husson, B., Skogen, M.D., Wallhead, P., 2023. Why do regional biogeochemical models produce contrasting future projections of primary production in the Barents Sea? J. Sea Res. 192, 102366. http://dx.doi.org/10.1016/j.seares.2023.102366.

Ottersen, G., Stenseth, N.C., 2001. Atlantic climate governs oceanographic and ecological variability in the Barents Sea. Limnol. Oceanogr. 46, 1774–1780. http://dx.doi.org/10.4319/lo.2001.46.7.1774.

Oziel, L., Baudena, A., Ardyna, M., Massicotte, P., Randelhoff, A., Sallée, J.-B., Ingvaldsen, R.B., Devred, E., Babin, M., 2020. Faster Atlantic currents drive poleward expansion of temperate phytoplankton in the Arctic Ocean. Nature Commun. 11, 1705. http://dx.doi.org/10.1038/s41467-020-15485-5.

Oziel, L., Massicotte, P., Babin, M., Devred, E., 2022. Decadal changes in Arctic Ocean chlorophyll a: Bridging ocean color observations from the 1980s to present time. Remote Sens. Environ. 275, 113020. http://dx.doi.org/10.1016/j.rse.2022.113020.

Pabi, S., van Dijken, G.L., Arrigo, K.R., 2008. Primary production in the Arctic Ocean, 1998–2006. J. Geophys. Res.: Oceans 113, http://dx.doi.org/10.1029/2007JC004578.

Pauly, D., Christensen, V., 1995. Primary production required to sustain global fisheries. Nature 374, 255–257. http://dx.doi.org/10.1038/374255a0.

Pavlov, A.K., Taskjelle, T., Kauko, H.M., Hamre, B., Hudson, S.R., Assmy, P., Duarte, P., Fernández-Méndez, M., Mundy, C.J., Granskog, M.A., 2017. Altered inherent optical properties and estimates of the underwater light field during an Arctic under-ice bloom of Phaeocystis pouchetii. J. Geophys. Res.: Oceans 122, 4939–4961. http://dx.doi.org/10.1002/2016JC012471.

Peralta-Ferriz, C., Woodgate, R.A., 2015. Seasonal and interannual variability of pan-Arctic surface mixed layer properties from 1979 to 2012 from hydrographic data, and the dominance of stratification for multiyear mixed layer depth shoaling. Prog. Oceanogr. 134, 19–53. http://dx.doi.org/10.1016/j.pocean.2014.12.005.

Perrette, M., Yool, A., Quartly, G.D., Popova, E.E., 2011. Near-ubiquity of ice-edge blooms in the Arctic. Biogeosciences 8, 515–524. http://dx.doi.org/10.5194/bg-8-515-2011.

Rat'kova, T.N., Wassmann, P., 2002. Seasonal variation and spatial distribution of phyto- and protozooplankton in the central Barents Sea. J. Mar. Syst. 38, 47–75. http://dx.doi.org/10.1016/S0924-7963(02)00169-0, seasonal C-cycling variability in the open and ice-covered waters of the Barents Sea.

Reigstad, M., Carroll, J., Slagstad, D., Ellingsen, I., Wassmann, P., 2011. Intra-regional comparison of productivity, carbon flux and ecosystem composition within the northern Barents Sea. Prog. Oceanogr. 90, 33–46. http://dx.doi.org/10.1016/j.pocean.2011.02.005, arctic Marine Ecosystems in an Era of Rapid Climate Change.

Reigstad, M., Wassmann, P., Wexels Riser, C., Øygarden, S., Rey, F., 2002. Variations in hydrography, nutrients and chlorophyll a in the marginal ice-zone and the central Barents Sea. J. Mar. Syst. 38, 9–29. http://dx.doi.org/10.1016/S0924-7963(02)00167-7, seasonal C-cycling variability in the open and ice-covered waters of the Barents Sea.

Renaut, S., Devred, E., Babin, M., 2018. Northward expansion and intensification of phytoplankton growth during the early ice-free season in Arctic. Geophys. Res. Lett. 45, 10590–10598. http://dx.doi.org/10.1029/2018GL078995.

Rey, F., 1991. Photosynthesis-irradiance relationships in natural phytoplankton populations of the Barents Sea. Polar Res. 10, 105–116. http://dx.doi.org/10.1111/j.1751-8369.1991.tb00638.x.

Rey, F., 2012. Declining silicate concentrations in the Norwegian and Barents Seas. ICES J. Mar. Sci. 69, 208–212. http://dx.doi.org/10.1093/icesjms/fss007.

Rudels, B., Meyer, R., Fahrbach, E., Ivanov, V.V., Østerhus, S., Quadfasel, D., Schauer, U., Tverberg, V., Woodgate, R.A., 2000. Water mass distribution in Fram Strait and over the Yermak Plateau in summer 1997. Ann. Geophys. 18, 687–705. http://dx.doi.org/10.1007/s00585-000-0687-5.

Sakov, P., Counillon, F., Bertino, L., Lisæter, K.A., Oke, P.R., Korablev, A., 2012. TOPAZ4: an ocean-sea ice data assimilation system for the North Atlantic and Arctic. Ocean Sci. 8, 633–656. http://dx.doi.org/10.5194/os-8-633-2012.

Sandven, H., Hamre, B., Petit, T., Röttgers, R., Liu, H., Granskog, M.A., 2023. Seasonality and drivers of water column optical properties on the northwestern Barents Sea shelf. Prog. Oceanogr. 103076. http://dx.doi.org/10.1016/j.pocean.2023.103076.

Schrum, C., Alekseeva, I., St. John, M., 2006. Development of a coupled physical–biological ecosystem model ECOSMO: Part I: Model description and validation for the North Sea. J. Mar. Syst. 61, 79–99. http://dx.doi.org/10.1016/j.jmarsys.2006.01.005.

Silva, E., Counillon, F., Brajard, J., Korosov, A., Pettersson, L.H., Samuelsen, A., Keenlyside, N., 2021. Twenty-one years of phytoplankton bloom phenology in the Barents, Norwegian, and North Seas. Front. Mar. Sci. 8, http://dx.doi.org/10.3389/fmars.2021.746327.

Slagstad, D., Ellingsen, I., Wassmann, P., 2011. Evaluating primary and secondary production in an Arctic Ocean void of summer sea ice: An experimental simulation approach. Prog. Oceanogr. 90, 117–131. http://dx.doi.org/10.1016/j.pocean.2011.02.009, arctic Marine Ecosystems in an Era of Rapid Climate Change.

Slagstad, D., Wassmann, P.F.J., Ellingsen, I., 2015. Physical constrains and productivity in the future Arctic Ocean. Front. Mar. Sci. 2, http://dx.doi.org/10.3389/fmars.2015.00085.

Søgaard, D.H., Sorrell, B.K., Sejr, M.K., Andersen, P., Rysgaard, S., Hansen, P.J., Skyttä, A., Lemcke, S., Lund-Hansen, L.C., 2021. An under-ice bloom of mixotrophic haptophytes in low nutrient and freshwater-influenced Arctic waters. Sci. Rep. 11, 2915. http://dx.doi.org/10.1038/s41598-021-82413-y.

Søreide, J.E., Hop, H., Falk-Petersen, S., Gulliksen, B., Hansen, E., 2003. Macrozooplankton communities and environmental variables in the Barents Sea marginal ice zone in late winter and spring. Mar. Ecol. Prog. Ser. 263, 43–64. http://dx.doi.org/10.3354/meps263043.

Stoer, A.C., Fennel, K., 2023. Estimating ocean net primary productivity from daily cycles of carbon biomass measured by profiling floats. Limnol. Oceanogr. Lett. 8, 368–375. http://dx.doi.org/10.1002/lol2.10295.

The Nansen Legacy, 2022. Sampling Protocols: Version 10, Vol. 32. Tech. Rep., UiT - Arctic University of Tromsø, Norway, http://dx.doi.org/10.7557/nlrs.6684, Nansen Legacy Report Series.

Uitz, J., Claustre, H., Morel, A., Hooker, S.B., 2006. Vertical distribution of phytoplankton communities in open ocean: An assessment based on surface chlorophyll. J. Geophys. Res.: Oceans 111, http://dx.doi.org/10.1029/2005JC003207.

Vader, A., 2022. Chlorophyll A and phaeopigments Nansen Legacy. data retrieved from http://dx.doi.org/10.21335/NMDC-1371694848.

Vernet, M., Ellingsen, I., Marchese, C., Bélanger, S., Cape, M., Slagstad, D., Matrai, P.A., 2021. Spatial variability in rates of net primary production (NPP) and onset of the spring bloom in Greenland shelf waters. Prog. Oceanogr. 198, 102655. http://dx.doi.org/10.1016/j.pocean.2021.102655.

Vernet, M., Ellingsen, I.H., Seuthe, L., Slagstad, D., Cape, M.R., Matrai, P.A., 2019. Influence of phytoplankton advection on the productivity along the atlantic water inflow to the Arctic Ocean. Front. Mar. Sci. 6, http://dx.doi.org/10.3389/fmars.2019.00583.

Vernet, M., Matrai, P.A., Andreassen, I., 1998. Synthesis of particulate and extracellular carbon by phytoplankton at the marginal ice zone in the Barents Sea. J. Geophys. Res.: Oceans 103, 1023–1037. http://dx.doi.org/10.1029/97JC02288.

Wassmann, P., 2011. Arctic marine ecosystems in an era of rapid climate change. Prog. Oceanogr. 90, 1–17. http://dx.doi.org/10.1016/j.pocean.2011.02.002, arctic Marine Ecosystems in an Era of Rapid Climate Change.

Wassmann, P., Reigstad, M., Haug, T., Rudels, B., Carroll, M.L., Hop, H., Gabrielsen, G.W., Falk-Petersen, S., Denisenko, S.G., Arashkevich, E., et al., 2006a. Food webs and carbon flux in the Barents Sea. Prog. Oceanogr. 71, 232–287. http://dx.doi.org/10.1016/j.pocean.2006.10.003.

Wassmann, P., Slagstad, D., Ellingsen, I., 2010. Primary production and climatic variability in the European sector of the Arctic Ocean prior to : preliminary results. Polar Biol. 33, 1641–1650. http://dx.doi.org/10.1007/s00300-010-0839-3.

Wassmann, P., Slagstad, D., Riser, C.W., Reigstad, M., 2006b. Modelling the ecosystem dynamics of the Barents Sea including the marginal ice zone II. Carbon flux and interannual variability. J. Mar. Syst. 59, 1–24. http://dx.doi.org/10.1016/j.jmarsys.2005.05.006.

Wold, A., H, H., Svensen, C., K, A., Søreide, E., Ormacyk, M., Kwasniewski, S., 2023. Atlantification influences zooplankton communities seasonally in the northern Barents Sea and Arctic Ocean. Prog. Oceanogr. In revision.

Yumruktepe, V.Ç., Samuelsen, A., Daewel, U., 2022. ECOSMO II(CHL): a marine biogeochemical model for the North Atlantic and the Arctic. Geosci. Model Dev. 15, 3901–3921. http://dx.doi.org/10.5194/gmd-15-3901-2022.